Validation of the Aeolus Level-2B wind product over Northern Canada and the Arctic

Chih-Chun Chou[1], Paul J. Kushner[1], Stéphane Laroche[2], Zen Mariani[2], Peter Rodriguez[2], Stella Melo[2], Christopher G. Fletcher[3]

[1]Department of Physics, University of Toronto, Toronto, M5S 1A7, Canada
[2]Environment and Climate Change Canada.
[3]Department of Geography and Environmental Management, University of Waterloo, Canada.

Correspondence to: Chih-Chun Chou (gina.chou@mail.utoronto.ca)

Abstract. In August 2018, the European Space Agency launched the Aeolus satellite, whose Atmospheric LAser Doppler INstrument (ALADIN) is the first spaceborne Doppler wind lidar to regularly measure vertical profiles of horizontal line-of-sight (HLOS) winds with global sampling. This mission is intended to assess improvement to numerical weather prediction provided by wind observations in regions poorly constrained by atmospheric mass, such as the tropics, but also, potentially, in polar regions such as the Arctic where direct wind observations are especially sparse. There remain gaps in the evaluation of the Aeolus products over the Arctic region, which is the focus of this contribution. Here, an assessment of the Aeolus Level-2B wind product is carried out from measurement stations in Canada's north, to the pan-Arctic, with Aeolus data being compared to Ka-band radar measurements at Iqaluit, Nunavut; to radiosonde measurements over Northern Canada; to Environment and Climate Change Canada (ECCC)'s short-range forecast; and to the reanalysis product, ERA5, from the European Centre for Medium-Range Weather Forecasts (ECMWF). Periods covered include the early phase ~~during~~of the first laser ~~nominal~~ flight model (FM-A; 2018-09 to 2018-10), the early phase ~~during~~of the second laser flight ~~laser~~model (FM-B; 2019-08 to 2019-09), and the ~~mid~~ middle phase of FM-B ~~periods~~ (2019-12 to 2020-01). The adjusted r-~~square~~squared between Aeolus and other local datasets are around 0.9, except for ~~somewhat~~ lower values in comparison with the ground-based radar, presumably due to limited sampling. This consistency degraded by about 10% for the Rayleigh winds in the summer~~, presumably~~ due to ~~scattering from the~~ solar background noise and other possible errors. Over the pan-Arctic, consistency, with correlation greater than 0.8, is found in the Mie channel from the planetary boundary layer to the lower stratosphere (near surface to 16 km a.g.l.) and in the Rayleigh channel from the troposphere to the stratosphere (2 km to 25 km a.g.l.). ~~Zonal and meridional projections of the HLOS winds are separated to account for the systematic changes in HLOS winds arising from sampling wind components from different viewing orientations in the ascending and descending phases.~~ In all ~~cases~~three periods, Aeolus standard deviations are found to be ~~20~~5 to 40% greater than those from ECCC-B and ERA5. We found that the L2B estimated error product for Aeolus is coherent with the differences between Aeolus and the other datasets, and can be used as a guide for expected consistency. Thus, our work confirms the quality of the Aeolus dataset over the Arctic and shows

that the new Aeolus L2B wind product provides a valuable addition to current wind products in regions, such as the Arctic Ocean region, where few direct wind observations have been available to date.

1 Introduction

A better characterization of the global wind field ~~would advance~~has the ~~initialization of~~ potential to improve numerical weather prediction (NWP) and thereby improve our knowledge of the ~~characteristics and~~ transport of moisture, energy, and other fields in the global atmosphere (Baker et al.,1995; Graham et al., 2000, Naakka et al., 2019). Altitude~~-~~-resolved wind observations are available from aircraft reports and surfaced-based observations ~~(e.g.,~~such as radiosondes and wind profilers~~)~~.. However, ~~those~~such observations are generally scattered and especially rare over large bodies of water ~~surfaces like~~such as the world's oceans, ~~and the~~ as well as over polar regions. Winds derived from passive space-based observations~~, such as~~ include atmospheric motion vectors (AMVs) ~~and spaceborne scatterometer, are retrieved~~estimated from the movements of clouds and water vapour (Velden et al., 2017; Mizyak et al., 2016) ~~or from scattering~~and surface winds from space-based scatterometer from the ocean surface. ~~Satellite-derived AMVs can~~ Although AMV products provide wind information ~~of winds~~ over multiple tropospheric layers using multispectral water vapor ~~capabilities~~remote sensing (Velden et al., 1997; Bormann and Thépaut, 2004; Le Marshall et al., 2008~~). Overall, AMV products~~), they lack precision in terms of altitude assignment and their sampling is limited to only a few levels~~, which~~. This limits ~~representation of~~how AMV's represent the small-scale vertical structure of the wind profile~~, for example.~~. Spaceborne scatterometers, on the other hand, are limited to ocean near-surface winds and their accuracy is therefore sensitive to surface weather conditions (Chiara et al., 2017; Young et al., 2017). Improving altitude-resolved winds from remote sensing on a global scale requires adoption of active sensors, which have only recently become feasible for deployment from space~~-~~-based platforms (Dabas, 2010).

On 22 August 2018, the European Space Agency (ESA) launched the Aeolus satellite carrying the first spaceborne Doppler wind lidar (DWL) designed to significantly improve altitude-resolved wind observations, from the surface to the stratosphere, on a global scale (Källen, 2018; Reitebuch et al., 2019). The instrument carries an emitting UV laser and two receivers to measure the Doppler shift from backscattering by air molecules (Rayleigh channel) and by aerosols or cloud particles (Mie channel). Aeolus was designed to improve global weather forecasts, with an emphasis on tropical winds, because tropical wind information is required to fully characterize the circulation when dynamical balance constraints are weak (Horányi et al., 2015). However, since it is polar orbiting, Aeolus also fills an observation gap in the polar regions, including the Arctic region, which is our focus. It is worthwhile exploring how ~~filling this gap~~new measurements of Arctic winds, along with other meteorological observations, might improve Arctic forecasts (e.g~~.,~~., Yamazaki et al., 2015), and, by extension, prediction outside the Arctic (Naakka et al., 2019; Lawrence et al., 2019), with a potential to influence forecasting and characterization of mid-latitude weather and climate extremes (Walsh et al., 2019; Cohen et al., 2020; Sato et al., 2017). We are thus motivated to ~~invest in understanding~~better understand the quality of Aeolus data products in the Arctic region, particularly for Canada, given its large territorial extent at high northern latitudes.

The purpose of this paper is to evaluate the quality of Aeolus wind products over ~~Northern~~northern Canada and the Arctic in comparison with several available observational products~~, including~~. We will focus on analyzing random errors instead of systematic errors since, as recommended for operational NWP practice, bias corrected Aeolus data is used in this study (see Sect. 2.1). The products compared include the dataset from the Canadian Arctic Weather Science (CAWS) project ~~supersites, that contain a suite of~~, which includes ground based remote sensing and in-situ instruments for enhanced meteorological observations~~ located at Iqaluit, NU (64° N, 69° W) and Whitehorse, YK (61° N, 135° W) (Joe et al., 2020). Because of data limitations (see below), only Iqaluit ground-based remote sensing data will be used in this study~~. As part of the Canadian contribution to the international calibration/validation effort for Aeolus (Martin et al., ~~2020~~2021; Guo et al., 2020; Baars et al., 2020), this project serves to test ~~new technologies and provide cost-effective alternatives~~the spaceborne DWL that provides alternative observational wind data to atmospheric monitoring over the northern regions. The CAWS "supersites" are located at Iqaluit, NU (64° N, 69° W) and Whitehorse, YK (61° N, 135° W) (Joe et al., 2020), but because of data limitations (see below), only Iqaluit ground-based remote sensing data, along with Whitehorse radiosonde data, will be used in this study.

In related Arctic-based work, Belova et al. (~~in review, ~~2021) have found consistency between Aeolus winds and a ground-based radar situated in northern Sweden with insignificant biases ~~and slight~~between the two products (less than 1 ms^{-1}) and slightly increased random errors for Aeolus in the boreal summer~~.~~, possibly due to sunlight scatter. We here ~~expand from~~build on this encouraging study by moving from ~~an in-situ~~a narrow focus ~~to specific~~at Iqaluit and Whitehorse, motivated by CAWS; to a broader set of radiosonde network locations ~~in~~across northern Canada, including Iqaluit and Whitehorse; and finally, to a pan-Arctic perspective. ~~We evaluate~~Products compared to the Aeolus wind products ~~co-located with 1) ground-based in-situ, radiosonde and remote sensing observations at the Iqaluit CAWS supersite; 2)~~include the Iqaluit Ka-band radar data; radiosonde ~~stations at the Iqaluit and Whitehorse sites and more broadly over Northern~~data across northern Canada~~;~~, including Iqaluit and ~~3)~~Whitehorse, and global data-assimilation based wind products, including the short-range forecast from ECCC's operational NWP system (ECCC-B) and the fifth major global reanalysis ~~produced by~~of the European Centre for Medium-Range Weather Forecasts (ECMWF ERA5). Section 2 provides a description of each of these datasets. Section 3.1 describes the ~~comparison during the early FM-A period (15 September to 16 October 2018) to ground-based measurements in Canada's North, including the~~validation against Iqaluit ~~supersite ~~and ~~radiosonde stations over the Northern Canada. Section~~the other Canadian Arctic sites, and Sect. 3.2 describes ~~the~~a broader validation for the ~~regions and periods of analysis over the~~ pan-Arctic ~~(poleward of 70° N) during the early FM-A period, early FM-B period (2 August to 30 September 2019),~~against background and ~~mid-FM-B period (1 December to 31 January 2020) for the Aeolus' near real-time (2B02/2B06) and reprocessed (2B10) wind~~reanalysis products. A summary and discussion of the results is provided in Sect. 4.

2 Datasets

We now discuss the Aeolus wind products (Sect. 2.1), the other datasets that will be compared with the Aeolus wind products (Sects. 2.2-2.4), and the data matching process including coincidence criteria used in the validation (Sect. 2.5).

2.1 Aeolus L2B HLOS wind product

The near polar-orbiting and sun-synchronous Aeolus satellite measures global atmospheric wind profiles along the DWL's line-of-sight (LOS) from the Earth's surface to the lower stratosphere (Straume et al., 2018). The LOS of Aeolus is perpendicular to its orbital velocity to mitigate contributions from its along-orbit velocity. ~~It points 35° from the nadir to capture a single component of the wind.~~ Its DWL, ~~named~~the Atmospheric LAser Doppler INstrument (ALADIN, Guo et al., 2020), points 35° from the nadir and includes two receivers to measure the Doppler shift from the emitting laser along the LOS: a double Fabry-Pérot spectrometer to measure Rayleigh scattering from air molecules and a Fizeau spectrometer to measure Mie scattering from cloud droplets and aerosols. The horizontal line-of-sight (HLOS) wind component can be derived by analyzing the Doppler frequency shift and assuming that the vertical component of winds is negligible. ~~In this section, we will discuss~~The wind retrieval method of the processed and calibrated Aeolus ~~wind product and the other datasets that will be compared with the Aeolus HLOS winds.~~

~~2.1 Aeolus~~ Level-2B (L2B) HLOS wind product

~~Aeolus's Level-2B (L2B) products comprise a fully calibrated and processed HLOS wind product, whose wind retrieval method~~ can be found in the Algorithm Theoretical Basis Documents (Rennie et al., 2020a). For both Mie and Rayleigh channels each measurement~~-~~ bin is classified into "cloudy" or "clear" using its optical property information from Level-1B scattering ratio estimates (Rennie et al., 2020a). "Cloudy" classification occurs when the measurement-bins have non-zero particle backscatter, while "clear" classification occurs for predominantly molecular backscatter. Since Mie-cloudy and Rayleigh-clear ~~wind results~~winds are considered as superior quality compared to Mie-clear and Rayleigh-cloudy winds (Martin et al., ~~2020~~2021; Guo et al., 2020; Baars et al., 2020), Mie winds and Rayleigh winds refer exclusively to Mie-cloudy and Rayleigh-clear winds in the rest of this study.

Formatted: Indent: First line: 1.27 cm

The backscattered signal must be horizontally and vertically averaged to ~~have~~obtain a sufficient signal-to-noise ratio (SNR) (Drinkwater et al., 2016; Reitebuch et al., 2019; Lux et al., 2020). ~~Stronger signal returns are expected from the Mie scattering than for~~Prior to 5 March 2019, both Rayleigh ~~scattering; therefore, the~~ and Mie winds were averaged to up to a horizontal resolution ~~is~~of 87 km. Recognizing that Mie scattering in cloudy air yields stronger returns than Rayleigh scattering in clear air, after 5 March 2019, the Mie wind product was provided at a finer ~~for the Mie winds (about 10 km) than for the Rayleigh winds (about 90 km). Similarly, the vertical~~horizontal resolution ~~depends on the signal strength of the measurements.~~

~~In~~of 12 km. The vertical resolution decreases from 500 m in the PBL (defined here as below 2 km in altitude~~), the vertical structure allows a finer vertical resolution (500 m). It decreases with altitude~~) to 1 km in the free troposphere (defined here as 2 to 16 km in altitude) and to 2 km in the lower stratosphere (above 16 km in altitude). The Mie channel covers the vertical range up to 16 km in altitude and the Rayleigh channel covers up to 30 km.

Aeolus switched from the first laser, flight ~~laser~~model A (FM-A) to the second laser, flight ~~laser~~model B (FM-B) due to a decrease in ultraviolet (UV) power output from FM-A at the end of June 2019 (Reitebuch et al., 2019; Lux et al., 2020). Aeolus L2B near real-time baseline products 2B02 and 2B06/07 are used during early FM-A period (~~fall~~ 15 September to 16 October 2018) and FM-B period (~~summer~~2 August to 30 September 2019 and ~~winter~~1 December 2019 to 31 January 2020) respectively. ECMWF has ~~recently~~ published the first reprocessed data in fall 2020 (2B10~~),~~; available at ftp://2018_aeolus_l2b:ecmwf@acquisition.ecmwf.int/), which covers the period between 24 June and 31 December 2019. The major improvement in this product is a daily updated bias correction accounting for variability of the temperature gradients across the detector telescope's primary M1 mirror ~~M1~~; additional improvements are mentioned below and in other studies (e.g., Rennie and Isaksen, 2020; Laroche and St. James ~~submitted to QJRMS).~~, 2021). A comparison of the statistical results during the overlapping period, (boreal) summer 2019, between 2B06 and 2B10 will be presented in this study.

The following data selection is carried out in this study:

- L2B product provides a validation flag of 1 (valid) or 0 (invalid) (de Kloe et al., 2016) associated with each range-bin in an observation, and we therefore screen out validation flag value 0 (Baars et al., 2020).
- The quality control recommendation following ~~the Guidance for Aeolus NWP Impact Experiments (~~Rennie and Isaksen, ~~2019), including the threshold~~(2020). The thresholds for L2B estimated observation errors~~.~~ during the FM-A period are 4.5 ms^{-1} for the Mie winds and 6.6 to 11 ms^{-1} for the Rayleigh winds, depending on the pressure level, and 5 ms^{-1} for the Mie winds and 8.5 to 12 ms^{-1} for the Rayleigh winds during the early FM-B period. For more details, please refer to Rennie and Isaksen (2020).
- We further reject the outliers by excluding ~~all the~~ data ~~when~~for which the difference between the observations and ECCC-B or ERA5 is greater than 30 ms^{-1}. This criterion was obtained from an initial comparison between Aeolus FM-A and ECCC-B (Laroche et al., 2019). The outliers represent less than 1% of all data; however, ~~the O-B (Observation minus Background)~~excluding them has an important influence because their magnitude could be as large as 150 ms^{-1}.

During the early FM-A period, a global constant bias offset of -1.35 ms^{-1} was added to the Mie winds to bring them into better agreement with the ECMWF model (Rennie and Isaksen, ~~2019~~2020). The Aeolus observation heights were also systematically increased by 250 m due to a known calibration issue ~~(Rennie and Isaksen, 2019).~~. The biases of FM-B HLOS arising mainly from the telescope primary mirror M1 temperature gradients (Rennie and Isaksen, 2020) should be corrected as

Formatted: Don't adjust right indent when grid is defined, Don't adjust space between Latin and Asian text, Don't adjust space between Asian text and numbers

Formatted: English (United Kingdom)

much as possible before any use for validation against other wind measurements or data assimilation. Fortunately, these biases vary mostly with the orbital node and latitude and partly with longitude and height, facilitating such bias correction. ECCC has developed a bias correction scheme similar to ~~the~~ ECMWF, as described in Rennie and Isaksen (2020); see Laroche and St. James (~~submitted to QJRMS).~~2021). It is a ~~dynamic~~look-up table bias correction based on the mean observation minus ~~ECCC-B~~ the "background ~~(O-B~~" short-range forecast from ECCC (see Sect. 2.2) from the previous 7 days, as a function of orbit phase and latitude. It is applied for both Rayleigh and Mie HLOS winds. For the Rayleigh HLOS winds, the correction is also a function of longitude, binned in 10 degrees latitude by 36 ~~degrees~~ degree longitude sectors.

To project the wind vector in a given dataset into the Aeolus HLOS, we use

$$v_{HLOS} = -u \sin\varphi - v \cos\varphi, \tag{1}$$

where v_{HLOS} is the HLOS wind component, u is the zonal wind component, v is the meridional wind component, and φ is the azimuth of the LOS. ~~This equation is used for all the datasets described below to obtain the HLOS winds.~~ Conversely, we can also project the HLOS wind vector into the west-east and north-south directions (Wright et al., ~~in review,~~ 2021) for some analysis (Sect. 3.2), using

$$v_{HLOS,u} = -v_{HLOS} \cdot \sin(\varphi), \tag{2}$$

$$v_{HLOS,v} = -v_{HLOS} \cdot \cos(\varphi). \tag{3}$$

To repeat, these quantities do not represent zonal and meridional components of the total wind field, but the zonal and meridional projection of the vector component of the wind along the HLOS of Aeolus.

2.2 ECCC-B: Short-range forecast (background) from ECCC

The "background" from ECCC, termed "ECCC-B", is the 9-h short-range forecast used in the operational four-dimensional ensemble-variational (4D-EnVar) data assimilation scheme (Buehner et al., 2015). The forecast model is the operational Global Environmental Multiscale (GEM) (McTaggart-Cowan et al., 2019) with 15 km horizontal grid spacing and 84 vertical levels. There are over 13 million observations assimilated daily during the periods examined in this study, which include data from infrared (56.1% of all observations assimilated) and microwave (27.7%) satellite sounders and imagers, aircraft (9.6%), atmospheric motion vectors (2.3%), radiosondes (2.1%), scatterometers (1.0%), near-surface observations (0.7%), and satellite-based radio occultation (0.4%). ~~ECCC-B~~The data used to compare with Aeolus winds in this paper is ~~then~~the assimilated data that is linearly interpolated to Aeolus measurement locations and times. For the linear interpolation between the model's grid points, the horizontal grid-spacing is 15 km and the vertical grid-spacing varies from approximately 100 m in the PBL to 1 km in the stratosphere (McTaggart-Cowan et al., 2019). The linear interpolation in time is between two consecutive model states, 15 min apart.

Formatted: Font: Verdana, Font color: Accent 1

2.3 Reanalysis ERA5

The ERA5 hourly data on 37 pressure levels from the ECMWF ~~has been considered~~is also used in this study in validating the Aeolus measurements. This dataset is based on a four-dimensional variational (4DVar) data assimilation using Cycle 41r2 of the IFS, which was introduced operationally in 2016. ~~It~~ERA5 provides hourly estimates of atmospheric, land, and oceanic climate variables, available from 1950 to present. Data is gridded in a regular latitude-longitude grid of 0.25 degrees. A further discussion of the ERA5 configuration can be found in Hersbach et al. (2018 and 2020). The process used to match ERA5 and Aeolus data will be discussed in Sect. 2.5.

2.4 Ground-based measurements at Iqaluit, Nunavut; Whitehorse, Yukon; and other radiosonde stations

The CAWS project, led by ECCC, aims to characterize and improve scientific understanding of Arctic weather, climate, and cryospheric systems through enhanced meteorological observation capacity (Joe et al., 2020; Mariani et al., 2018). It also seeks to improve weather forecasts in the Canadian Arctic, test new technologies, and calibrate and validate space-based observations. ECCC's Iqaluit and Whitehorse sites (Fig. 1), so-called "supersites", were identified as "hot spots" for both extreme weather and transportation infrastructure that merited additional instrumentation. They provide researchers and forecasters with real-time weather observations which can be used in evaluating NWP models. Connected to ECCC's observational science mission, locating these weather stations at high latitudes also tests the ability of the coordinated instrument suites to operate in extreme cold conditions.

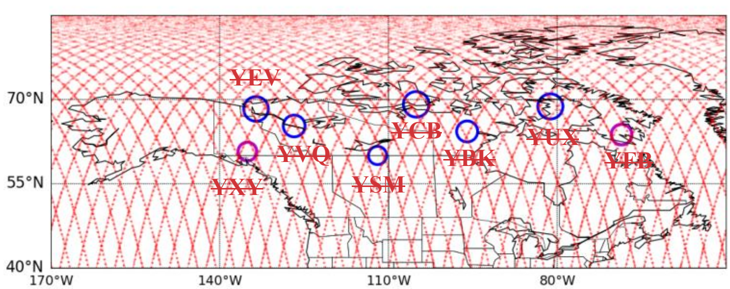

The Iqaluit site is situated in a valley to the north-east overlooking Frobisher Bay in the vicinity of 300 m hills. There are three instruments at Iqaluit site that provide wind profiles measurements: the radiosonde, Ka-band radar, and Doppler lidar. Vaisala RS92 radiosondes (Mariani et al., 2018) were launched twice daily (45 minutes before synoptic times 00 and 12

Coordinated Universal Time (UTC)). They measure vector wind profiles with a vertical resolution of roughly 15 m depending on ascent speed, up to about 30 km above ground level. The data used (available at http://weather.uwyo.edu/upperair/sounding.html) is the processed radiosonde data provided at mandatory and significant pressure levels (which has a coarser resolution than 15 m). It takes about two hours to reach 30 km altitude (around 10 hPa). The instrumental uncertainty for the wind speed is between 0.4 and 1.0 ms^{-1} and between 0.3 and 0.7 ms^{-1} for the zonal wind component (Dirksen et al., 2014). The error on the zonal wind component due to drift and elapsed time of the ascending balloon is between 0.5 and 1.0 ms^{-1} in the troposphere and UTLS (see Fig.5b in Laroche and Sarrazin, 2013). As a result, the total error for the zonal wind component from these sources of errors is between 0.6 and 1.2 ms^{-1}. Note that the radiosonde data are assimilated in the ECCC and ECMWF systems, which means that the ECCC-B and ERA5 errors are not independent of the radiosonde observation errors. The ECCC Whitehorse site, situated in a wide valley with large lakes, also has radiosondes that operate similarly to the ones at the Iqaluit.

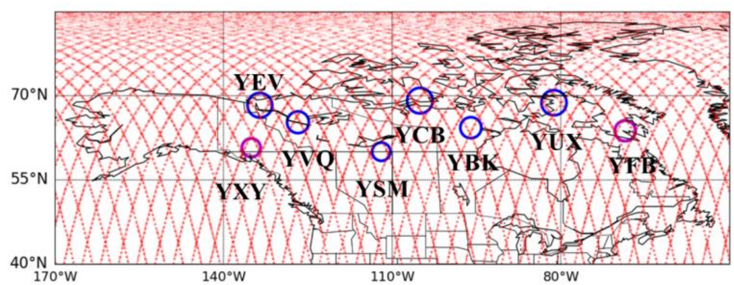

Figure 1. Aeolus's overpasses centred over northern Canada (red dots) during the first week of August 2019. The magenta 90-km radius circles centred on Iqaluit (YFB) and Whitehorse (YXY) within which coincident Aeolus overpasses were compared with other datasets (some circles appear differently sized because of map-projection distortion). The blue circles indicate the locations of other radiosonde stations over the Canadian Arctic: Inuvik (YEV), Fort Smith (YSM), Hall Beach (YUX), Cambridge Bay (YCB), Norman Wells Ua (YVQ), and Baker Lake (YBK).

~~The Iqaluit site is situated in a valley to the north-east overlooking Frobisher Bay in the vicinity of 300 m hills. There are three instruments at Iqaluit site that provide wind profiles measurements: the radiosonde, Ka-band radar, and Doppler lidar. Vaisala RS92 radiosondes (Mariani et al., 2018) were launched twice daily at 00 and 12 Coordinated Universal Time (UTC). They measure vector wind profiles with a vertical resolution of roughly 15 m (depending on ascent speed) up to about 30 km above ground level. The ECCC Whitehorse site, situated in a valley between two mountains, also has the radiosondes that operate similarly to the ones at the Iqaluit.~~

Formatted: Font: 9 pt

Formatted: Font: 9 pt

Formatted: Font: 9 pt

The dual-polarization cloud Doppler Ka-band radar at Iqaluit measures the LOS wind speed, fog backscatter, and depolarization ratio every 15 minutes. The radar measures the LOS wind with 14 m resolution and the LOS range goes from 5 to 30 km, depending on hydrometeor concentration. The uncertainty of the measurements depends on conditions, SNR, and decibel of the return signal. The average vertical wind profile bias to radiosonde is better than 0.27 ms^{-1}. The horizontal winds are derived using a high angle plan position indicator (PPI) 75 degrees scan using the VAD (Velocity-Azimuth-Display) algorithm (Lhermitte and Atlas, 1962; Wang et al., 2010). In other words, it is scanning with a fixed elevation angle (φ) while the azimuth angle (θ) is varied and is known function of time. The radial velocity is given by

$$v_r = u \sin\theta \, cos\varphi + v \cos\theta \cos\varphi + w \sin\varphi, \quad (4)$$

where w is the vertical wind component. By fitting the data and assuming uniform winds at each range, these three unknown parameters can be derived at each vertical level.

Lastly, the Doppler lidar measures the LOS component of wind and, ~~similar~~similarly to the radar, can retrieve horizontal winds via the VAD method. However, it is used only for visual comparison in this study (in the example profiles of Fig. 2) because it has very few coincident measurements with Aeolus due to its small vertical range, about 3 km a.g.l. or the cloud base height. Nevertheless, the Doppler lidar wind-profile observations were found to have measurements consistent with high-resolution radiosondes (Mariani et al., 2020), which should be borne in mind when considering our validation of Aeolus against radiosondes.

Other than the ECCC supersites, we also validate the Aeolus wind product ~~to the~~in comparison with radiosonde measurements over the Canadian Arctic at ground stations in Inuvik, Fort Smith, Hall Beach, Cambridge Bay, Norman Wells Ua, and Baker Lake (Fig. 1). They operate similarly to the radiosondes at ~~the supersites~~Iqaluit and Whitehorse and measure vector wind profiles. Some of the stations launch the radiosondes four times a day at 00, 06, 12, and 18 UTC. However, this does not affect the temporal criteria (see Sect. 2.5).

2.5 ~~Coincidence~~ Data matching process and coincidence criteria

For the ground-based validation, the criterion for coincidence of Aeolus overpasses is that the distance from the sites to the measurements ~~is~~be no more than 90 km (horizontal resolution of ~~Aeolus~~ Rayleigh winds). Using this coincidence criterion, Aeolus overpasses are selected as targets for validation at Iqaluit three times a week at around 21:50, 11:15, and 22:00 UTC, and at Whitehorse twice a week at around 02:25 and 15:30 UTC. The Aeolus measurements are compared to the reanalysis and in-situ measurements that are available in the nearest time. ~~Thus,~~Temporal sampling for each product is as follows: Aeolus overpasses at Iqaluit and Whitehorse are as mentioned above; reanalysis data is provided hourly, on the ~~temporal criterion is different for different instruments. The~~ hour; radiosonde data is from launches at 00 and 12 UTC, with a two-hour time-of-flight to 30 km as mentioned above; Ka-band radar data is provided via 15-minute scans. For example, if Aeolus overpasses selected as a target for validation at the Iqaluit site at 11:15 UTC, since the reanalysis data is sampled hourly, the radiosondes are launched at 00 and 12 UTC~~. Fortunately, the Aeolus overpasses North America around these times and overpasses Asia around 06 and 18 UTC. Therefore, although the radiosondes have poor temporal resolution, the nearest measured~~, and the Ka-band radar at Iqaluit scans every 15 minutes, the Aeolus HLOS profile would be compared to the ~~Aeolus~~reanalysis data and radiosonde measurements ~~is within one to two hours. However~~at 12 UTC and to the nearest scan by the radar. On the other hand, if the overpass time is 02:25 UTC, the profile would be compared to the ERA5 data at 02 UTC, the radiosonde measurements ~~are sometimes missing when the weather condition does not permit launching the sonde (e.g., high surface winds). The Ka-band radar at Iqaluit scans every 15 minutes. By taking the closest time, the temporal criterion for the radar is 7.5 minutes. We then compare these in-situ measurements to the bias-corrected and quality-controlled Aeolus measurements using the three processes of data selection as described above~~at 00 UTC, and, again, the nearest scan by the radar.

3 Results

3.1 Validation against ground-based measurements in the Canadian Arctic

We evaluated the vertical HLOS wind profile observations from coincident Aeolus overpasses for Iqaluit and Whitehorse against ground-based measurements, ECCC-B, and reanalysis. Our evaluation was limited to the early FM-A ~~phase~~period of Aeolus because the Ka-band radar at Iqaluit has been turned off for repairs since 1 August 2019. Figure 2 shows examples of

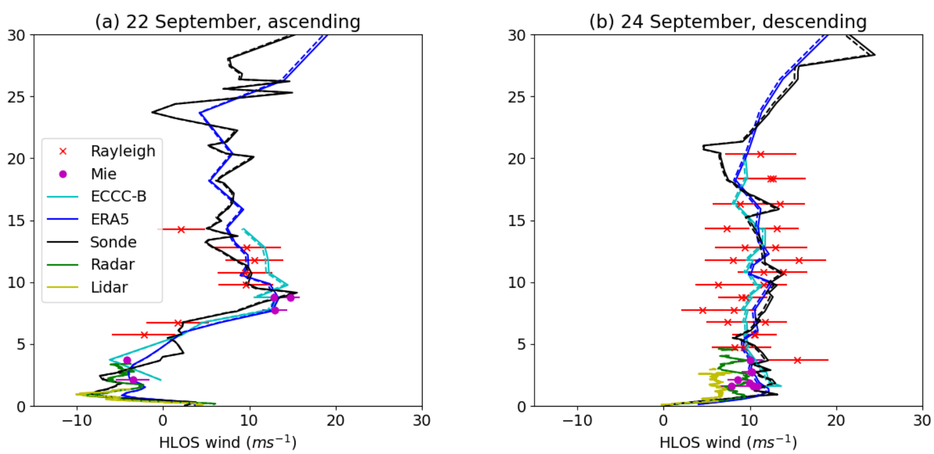

wind

~~Figure 2. HLOS wind~~ profile ~~observations from 1) coincident Aeolus overpasses (Rayleigh and Mie winds, along with L2B estimated error, i.e. wind error quantifier for each observation, 2) ECCC-B, i.e. the short-range forecast (background) from the ECCC numerical weather prediction model, 3) ERA5, and 4) ground-based remote sensing observations (radiosonde, Ka-band radar, and lidar measurements), on (a) September 22nd and (b) September 24th, 2018. Also shown are zonal component of the HLOS winds (dashed line). The HLOS winds are plotted so that their zonal component is positive eastward.~~

~~profile~~ measurements on (a) 22 September when Aeolus was in its ascending orbit phase and (b) 24 September 2018 when Aeolus was in its descending orbit phase, at the Iqaluit site. The HLOS wind profile is shown, along with profiles of the zonal projection of the HLOS component (dashed curves), $v_{HLOS,u}$ from equation (2), for ERA5, radiosonde, Ka-band radar, and lidar. When the measured HLOS winds are positive westward, i.e., when Aeolus is in its ascending ~~orbits~~orbit phase, we plot the profile of negative HLOS winds to ease the interpretation. The Ka-band radar's vertical range extends to less than 5 km in both profiles, around where there are Mie wind measurements from Aeolus, because its vertical range depends on hydrometeor concentration; the lidar's vertical range only extends to around 2 to 3 km. Due to the limited region of comparison, the agreement between Aeolus and radar is less good as we will discuss later, and we will not consider the lidar measurements further in this study.

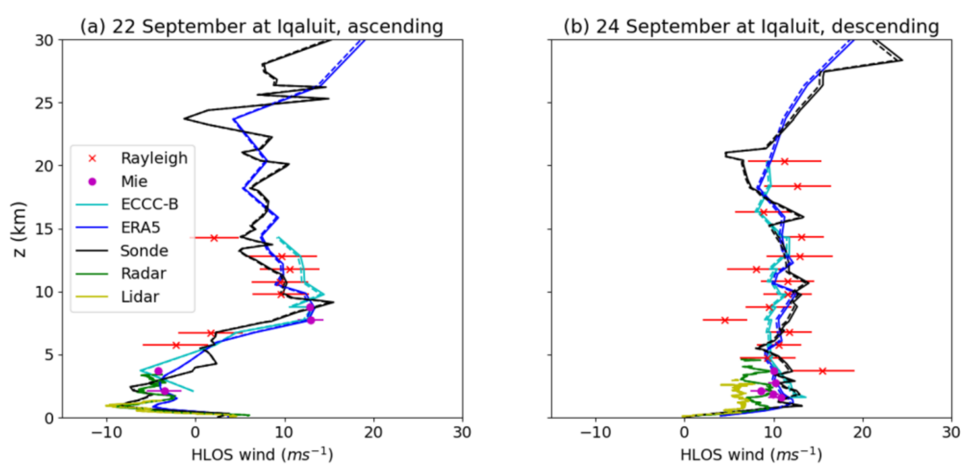

Figure 2. HLOS wind profile observations from coincident Aeolus overpasses (Rayleigh and Mie winds, along with L2B estimated error, i.e., wind error quantifier for each observation); ECCC-B, i.e., the short-range forecast (background) from the ECCC numerical weather prediction model; ERA5; and ground-based remote sensing observations (radiosonde, Ka-band radar, and lidar measurements), on (a) 22 September and (b) 24 September 2018. Also shown are zonal component of the HLOS winds (dashed line). The HLOS winds are plotted so that their zonal component is positive eastward.

~~It can be seen that~~

Aeolus consistently captures some of the basic structure of the wind profiles compared to in-situ measurements, ERA5 reanalysis, and ECCC-B. Because the ~~structure of the~~ solid lines ~~is~~lie very ~~similar~~close to the dashed lines, it is evident that

Formatted: Font: 9 pt
Formatted: Font: PMingLiU, English (United Kingdom)
Formatted: English (United Kingdom)
Formatted: Font: 9 pt
Formatted: Font: 9 pt, English (United Kingdom)
Formatted: Font: 9 pt
Formatted: Font: 9 pt
Formatted: Font: 9 pt, English (United Kingdom)

Aeolus is providing predominantly zonal wind information even at high latitudes (63° N) where the LOS has a greater meridional component than at low latitudes. On 22 September, Aeolus detects an easterly wind feature in the lower atmosphere and accurately picks up the change of sign around 5 km altitude. On 24 September, ~~Aeolus~~although a few of the Rayleigh measurements have a deviation close to 50%, Aeolus still measures westerly winds in reasonable overall agreement with the other data.

Figures 3 and 4 show scatter plots between the different datasets with lines of best fit and their range, and frequency distributions in percentage around Iqaluit (black) and Whitehorse (blue) sites. Figure 3 compares ~~Aeolus~~ Rayleigh ~~Clear~~ winds against the other products and Fig. 4 compares ~~Aeolus~~ Mie ~~Cloudy~~ winds against the other products. Aeolus provides more Rayleigh measurements than Mie winds during fall 2018, because the Rayleigh channel measures winds under clear-sky conditions and has greater vertical extent, while the Mie channel measures winds under cloudy or high-aerosol conditions.

To measure consistency of vertical profiles, we calculate the adjusted r-squared statistic, r^2_{adj}, using

$$r^2 = 1 - \frac{\sum_i (y_i - \hat{y}_i)^2}{\sum_i (y_i - \bar{y})^2}, \qquad (5)$$

$$r^2_{adj} = 1 - \frac{(1-r^2)(N-1)}{N-p-1}, \qquad (6)$$

where y_i is the Aeolus measurements (or other dataset shown on the y-axis), $\hat{y}_i$ is the estimated HLOS wind using linear regression, $\bar{y}$ is the mean of y, N is the total number of measurements, and p is the number of profiles. ~~The r^2_{adj} are shown in each panel legend in brackets.~~ The adjustment avoids overestimating the raw correlation from the scatterplots by accounting for within-profile agreement.

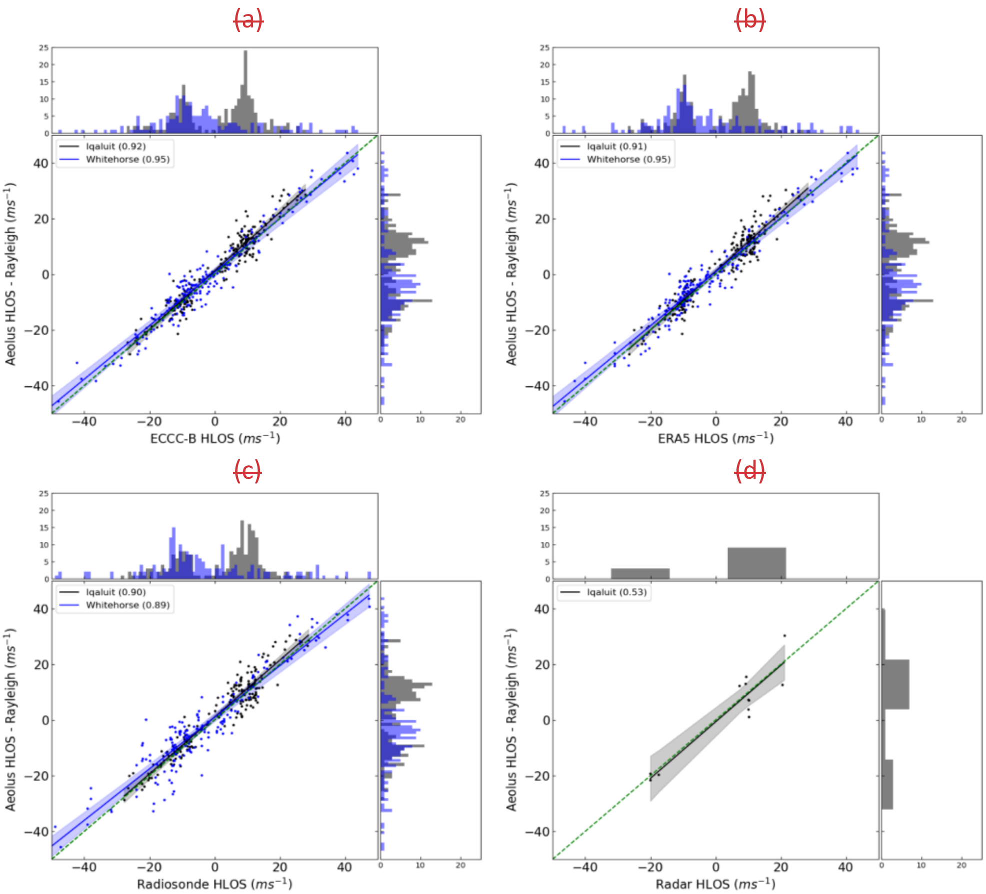

~~**Figure 3.** Scatter plots between Aeolus Rayleigh winds and (a) background, (b) ERA5, (c) radiosondes, and (d) Ka-band Radar and frequency distributions in percentage around Iqaluit and Whitehorse supersites during the early FM-A period. The numbers in brackets are the adjusted r-square between datasets whose degrees of freedom are the number of profiles during the period of analysis.~~ The N and p to calculate the adjusted r-squared in Figs. 3-4 are shown in Table S1. The r^2_{adj} and slope of the fitted line are shown in Table 1.

~~Overall, the datasets show strong consistency. ECCC-B and ERA5 are highly mutually consistent (Figure S1a; with adjusted r-squared greater than 0.97) and therefore show similar consistency with Aeolus (Fig. 3a-b and 4a-b). The ECCC-B has correlation of 0.92 and 0.95 with Aeolus Rayleigh winds and 0.87 and 0.98 with Aeolus Mie winds at Iqaluit and~~

Formatted: Line spacing: single

~~Whitehorse sites respectively. The ERA5 shows somewhat slightly lower correlation: 0.91 and 0.95 with Rayleigh winds and 0.81 and 0.99 with Mie winds. This difference might be attributed to enhanced resolution and sampling in ECCC-B compared to ERA5: ECCC-B features fine horizontal resolution (15 km grid) and vertical resolution (84 vertical levels) and a relatively~~

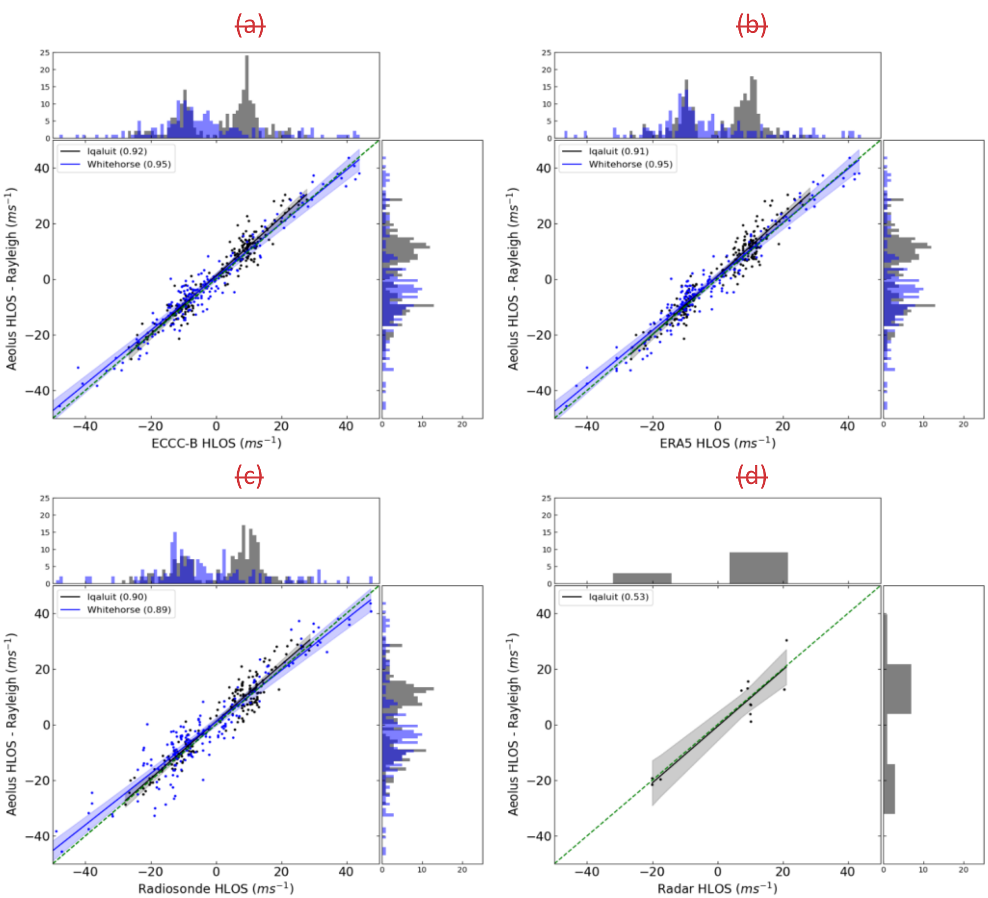

~~short (15-minute) time step.~~

~~**Figure 4.** Similar to Figure 3, but scatter plots between Aeolus Mie winds and other datasets.~~

Formatted: Font: 9 pt

Along with the consistency between ECCC-B and ERA5, these two datasets are also consistent with the radiosonde data ~~(Fig. S1), which is~~as expected, because radiosonde measurements are used in the operational ECCC and ECMWF data assimilation systems. All adjusted r-squared values in this comparison are above 0.95 for both sites.

	r_{adj}^2	**Slope**
Aeolus Rayleigh vs. ECCC-B	0.92 (0.95)	1.05 (0.96)
Aeolus Rayleigh vs. ERA5	0.91 (0.95)	1.05 (0.97)
Aeolus Rayleigh vs. radiosondes	0.90 (0.89)	1.02 (0.92)
Aeolus Rayleigh vs. radar	0.53	1.01
Aeolus Mie vs. ECCC-B	0.87 (0.98)	1.05 (0.98)
Aeolus Mie vs. ERA5	0.81 (0.99)	1.02 (1.01)
Aeolus Mie vs. radiosondes	0.82 (0.99)	1.01 (1.01)
Aeolus Mie vs. radar	0.66	1.00
ECCC-B vs. ERA5	0.97 (0.99)	0.99 (1.01)
ECCC-B vs. radiosondes	0.95 (0.95)	0.96 (0.98)
ERA5 vs. radiosondes	0.98 (0.97)	0.97 (0.98)

Table 1. Information on the adjusted r-squared and slope of fitted line from Figs. 3-4 as well as the comparisons between ECCC-B, ERA5, and radiosondes at Iqaluit, with values for Whitehorse shown in parentheses.

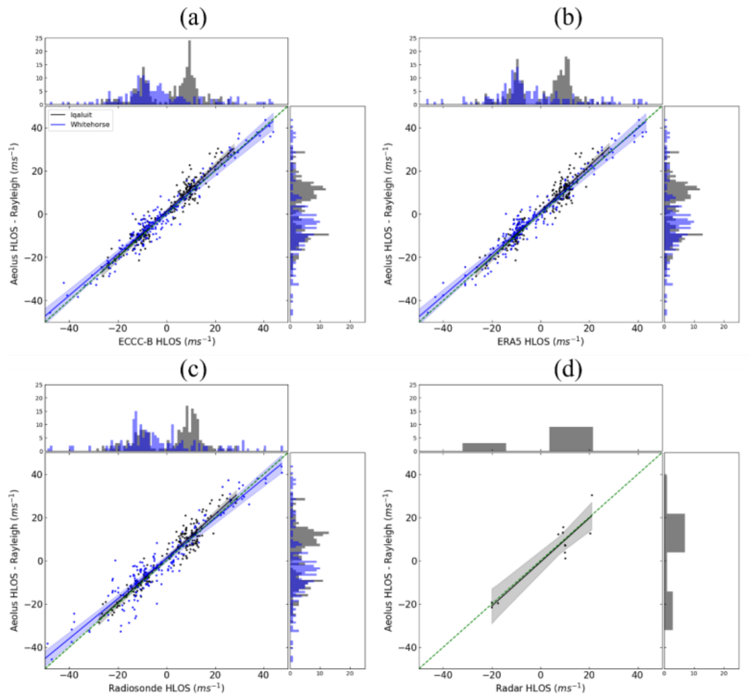

Figure 3. Scatter plots between Aeolus Rayleigh winds and (a) background, (b) ERA5, (c) radiosondes, and (d) Ka-band Radar and frequency distributions in percentage around Iqaluit and Whitehorse supersites during the early FM-A period.

Overall, the datasets show strong consistency. ECCC-B and ERA5 are highly mutually consistent (Table 1; with adjusted r-squared greater than 0.97) and therefore show similar consistency with Aeolus (Figs. 3a-b and 4a-b). -It can be seen that Aeolus Mie winds are less consistent with ECCC-B, ERA5, and radiosondes at Iqaluit than the corresponding observations at Whitehorse and for the Rayleigh winds. One possible reason for this relates to the fact that the Mie channel samples winds in the lower atmosphere where winds are harder to assimilate or measure due to topography. Since Iqaluit is situated in tundra valleys with rocky outcrops that can cause increased variability in the wind field while Whitehorse is situated in large valleys with less wind variability due to topography, terrain effects might account for the difference in consistency. In addition, the overall range extent of the HLOS wind samples is between -25 to 25 ms^{-1} at Iqaluit and -45 to 45 ms^{-1} at Whitehouse and r-squared is sensitive to the range of data (note the denominator of the second term in Eq. (5)). Overall, Aeolus data show good agreement with these three datasets with adjusted r-squared greater than 0.8.

Formatted: Line spacing: single

On the other hand, the adjusted r-squared between Aeolus winds and Ka-band radar at Iqaluit are only 0.53 for Rayleigh winds and 0.66 for Mie winds. As mentioned ~~earlier~~above, this might reflect a sampling bias because the vertical range of the instrument is relatively limited due to ~~the atmospheric composition and~~requirement for hydrometeors to be present, so that there are therefore relatively few points to sample. In addition, at larger ranges, the radar measures winds further from the radar and so the radar's measurement covers a larger volume. The validity of the assumption of uniform winds for the VAD calculation to be correct becomes less accurate as the range increases. However, we are comparing the VAD wind profile to a large distance along the track (87 km~~ for Rayleigh winds and 12 km for the FM-B Mie winds with around 15 m of laser footprint near the ground~~) as well, so this might not be the main cause. ~~Another~~Terrain effects at Iqaluit, mentioned above, might be another possible issue~~ could be the topography. The lower altitudes where we have radar (and lidar) observations are heavily influenced by local topography that can cause increased variability in the wind field. Therefore, the worse agreement with the 87 km averaged wind observations from~~: Aeolus might ~~arise from the fact that Aeolus "averaged~~average out~~" or filtered out the~~ wind variability due to the topography over ~~this large 15 × 87000 m region for the Rayleigh winds.~~the resolution provided by the HLOS products. This ~~demonstrates an important~~ reflects the challenge involved when comparing ~~two spatial averaged~~ measurements ~~that are not exactly collocated.~~with distinctive spatial sampling and limited coincidence. Generally, the sampling for these radar measurements ~~from radar~~ is highly limited, which tends to reduce the agreement

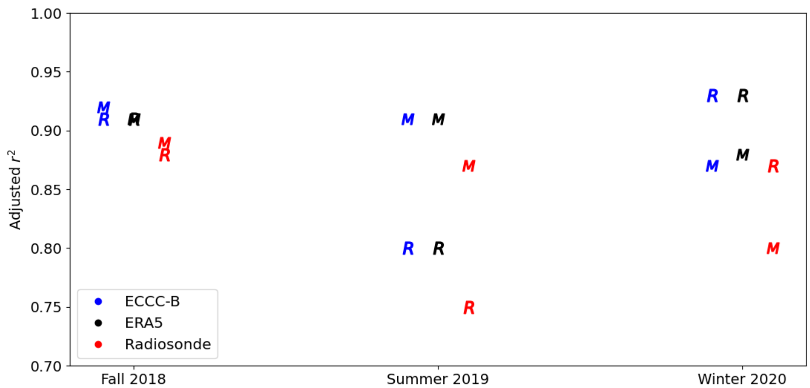

compared to the other datasets~~; nevertheless, the radar continues~~. Nevertheless, the agreement on the variances between Aeolus and the Ka-band radar is at 99% confidence level using F-test. This analysis highlights the importance for programs such as CAWS to continue to provide ~~a valuable~~ground-based radar measurements to ensure independent ~~measure~~measurements of the winds for future DWL missions.

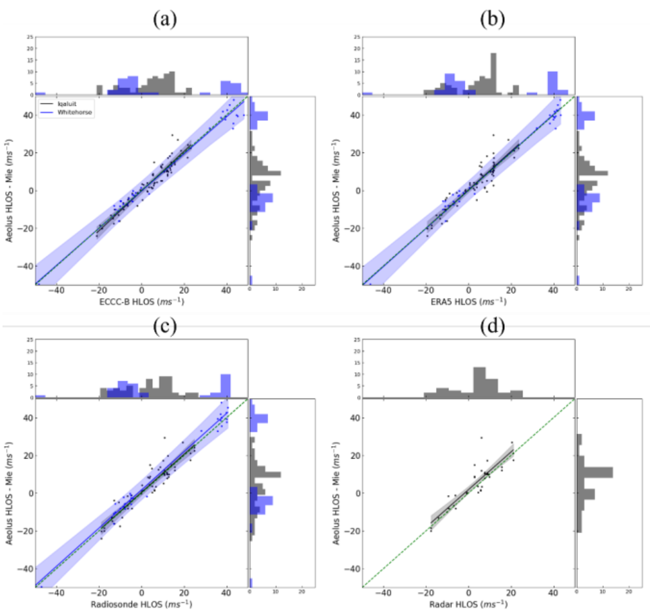

Figure 4. Similar to Figure 3, but scatter plots between Aeolus Mie winds and other datasets.

Formatted: Font: 9 pt

~~**Figure 5.** Adjusted r-squared of vertical HLOS wind profiles from coincident Aeolus (Rayleigh, R, and Mie, M) overpasses near radiosonde stations over the Canadian Arctic (shown in Figure 1) and ECCC-B, ERA5, and radiosonde measurements during fall 2018 (early FM-A), summer 2019 (early FM-B), and winter 2020 (mid-FM-B).~~

We broaden the region of analysis to the Canadian Arctic by incorporating all available Canadian Arctic radiosonde stations that provide wind profile observations. Figure 5 shows a comparison of adjusted r-squared (*N* and *p* are shown in Table S2) between 2B02/~~2B06~~06/07 Aeolus and ECCC-B, ERA5, and radiosonde measurements coincident with the radiosonde stations shown in Fig. 1, during early FM-A, early FM-B, and mid-FM-B periods. Aeolus wind profiles are less consistent ~~(dropped by around 5%)~~ with radiosonde measurements than with ECCC-B and ERA5 for both Rayleigh and Mie ~~channels~~winds during all three periods of analysis~~. This might have been anticipated given that~~ (adjusted r-squared values in the range 0.01-0.05 lower for the radiosonde ~~sampling~~observations). These results are in good agreement with those of Martin et al. (2020), who showed that the representativeness error is ~~more localized and thus more susceptible to discrepancies arising from lack of coincidence, compared to Aeolus and the analyses, which feature sampling over a~~significantly larger ~~spatial region.~~for radiosonde observations than those for the ECMWF and ICON models.

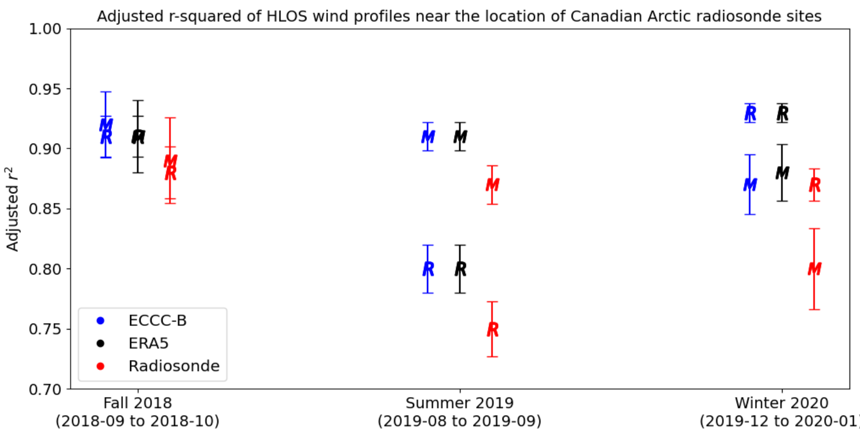

Figure 5. Adjusted r-squared of vertical HLOS wind profiles with 99% confidence level from coincident Aeolus (Rayleigh, R, and Mie, M) overpasses near radiosonde stations over the Canadian Arctic (shown in Figure 1) and ECCC-B, ERA5, and radiosonde measurements during fall 2018 (early FM-A), summer 2019 (early FM-B), and winter 2020 (mid-FM-B).

A systematic difference between the three measurement periods is apparent. Rayleigh winds could be very sensitive to the solar background ~~noise~~radiation (SBR) that contaminates the weak Rayleigh backscatter signal under clear sky condition. Random errors caused by the ~~solar background radiation (~~SBR~~)~~ were anticipated. Aeolus points towards the sun-synchronous night-side of its orbit to minimize the impact of SBR on the wind observations (Kanitz et al., 2019; Zhang et al., 2020). However, the impact is greater than expected, especially during summertime over the Arctic where the Rayleigh random errors can be as high as 8 ms^{-1} (Zhang et al., 2019; Krisch et al., 2020, Reitebuch et al., 2020). As a result, as will also be shown below, the consistency of Aeolus Rayleigh winds with other datasets markedly worsens during summer. We also note a slight drop in consistency of the Mie winds for the mid-FM-B period, which took place in winter 2020: for instance, the adjusted r-squared and their 99% confidence intervals, between Mie winds and ECCC-B, are 0.92$\pm$0.03 during fall 2018, 0.91$\pm$0.01 during summer 2019, and 0.87$\pm$0.02 during winter 2020. This decrease in the consistency is almost insignificant.

3.2 Pan-Arctic validation against background and reanalysis products

~~We now broaden our analysis even further to~~For more insight into how the behavior in the Canadian datasets we have examined extends to other Arctic regions, we now evaluate Aeolus wind measurements over the whole Arctic~~,~~ (measurement and profile counts provided in Table S3), including over the Arctic Ocean, where wind observations are particularly sparse. We evaluate the HLOS winds in relation to the ECCC-B and ERA5 products poleward of 70° N. Note that we exclude the measurements over a region that partially covers Greenland, North Atlantic Ocean, and Iceland (50° W to 5° E and 52.5° N to 80° N) in September 2019 because Aeolus had a different range bin setting over this area for AVARTAR-I campaign purposes (Fehr et al., 2020). The time-series of the estimated errors from 2B06 (solid line) and 2B10 (dashed line) datasets and the root-mean-square difference (RMSD) between the Aeolus Rayleigh winds and ECCC-B data are shown in Fig. 6. The estimated errors and RMSD over the excluded region (blue) have a sudden jump on 9 September ~~9th~~ while the rest of the Arctic (black) shows a consistent decrease in estimated errors and RMSD. The reprocessed data has improved estimated errors and RMSD over the excluded region; however, the jump is still visible. During this period, the satellite was measuring at a finer vertical resolution to compare with research-flight measurements. Thus, the derived winds were averaging over fewer measurements. The Rayleigh winds are particularly noisy due to the loss in optical signal on the atmospheric and internal path (Reitebuch et al., 2020), which emphasizes the seasonal variation of the solar background noise during boreal summer and perhaps also reflects the attempt to measure finer vertical scales. Thus, as a trade-off of having high vertical resolution, the Aeolus estimated errors are larger for this specific range bin setting. For the consistency of the data quality, we thus exclude the measurements for this period and region from subsequent analysis.

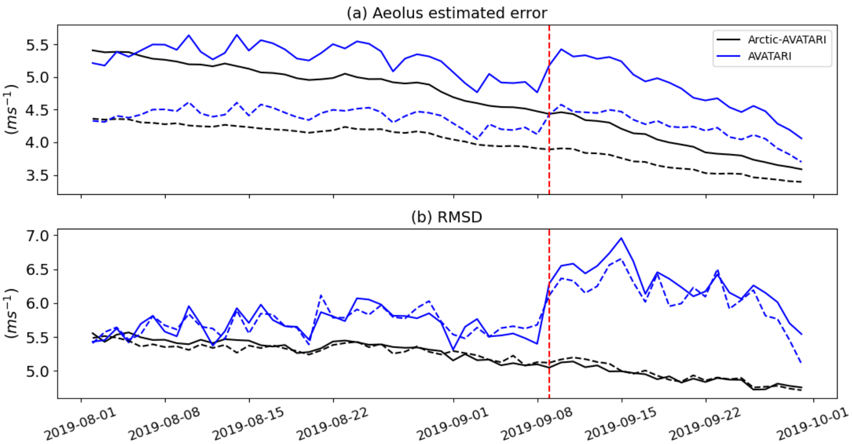

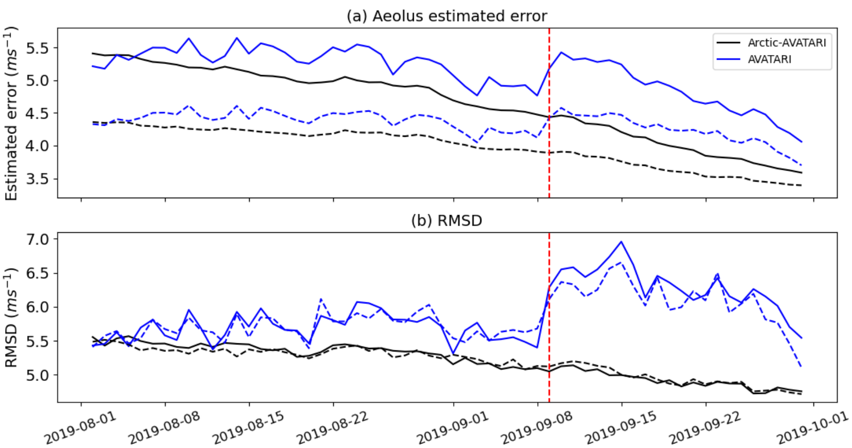

Figure 6. Time-series of (a) Aeolus L2B estimated error of Rayleigh winds and (b) RMSD between the ECCC-B and Aeolus 2B06 (solid) and 2B10 (dashed) data from 2 August to 30 September 2019. The data is averaged over the region with a different range bin setting for the AVATAR-I campaign (blue) and over the rest of the Arctic (black).

Formatted: Font: Bold

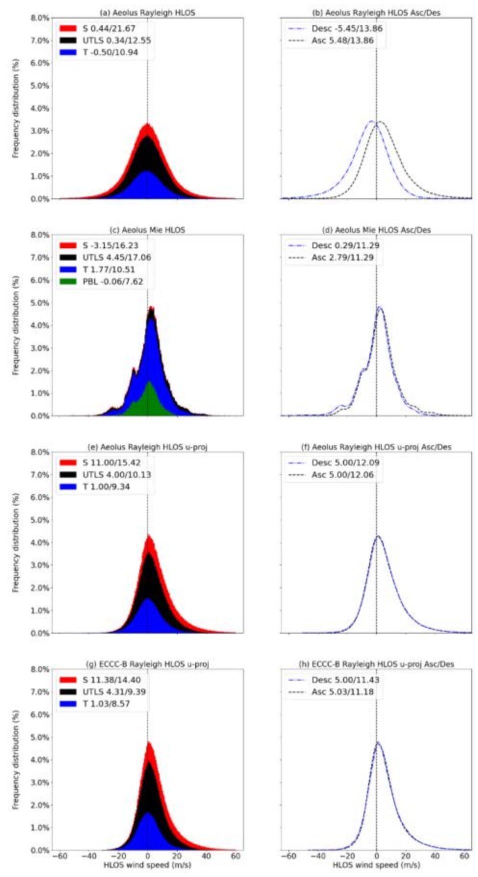

Figure 7. Aeolus Rayleigh ((a) and (b)) and Mie ((c) and (d)) HLOS measurement frequency distributions (%) during winter 2020 over the Arctic (>70° N). The HLOS winds are projected onto the east-west directions ((e) to (h)) from Aeolus measurements and ECCC-B HLOS winds. The panels on the right show the distribution of ascending and descending measurements separately. The means and standard deviations of distributions in each atmospheric layer are listed in the figure legends.

Formatted: English (United Kingdom)

Formatted: Left, Indent: First line: 0 cm, Line spacing: single

By expanding the region of analysis, we obtain a larger sample, which allows us to look at the separate ascending and descending orbit phases, frequency distributions in different layers in the atmosphere, correlations along the Aeolus track in different atmospheric layers, and the geographic variation of correlations between vertical HLOS profiles. We define four atmospheric layers: the planetary boundary layer (PBL, in the vertical range up to 2km), the free troposphere (T, 2-8 km), the upper troposphere/lower stratosphere (UTLS, 8-16 km), and the stratosphere (S, altitudes greater than 16 km). Rayleigh winds are more frequently sampled in the UTLS and the stratosphere since often cloud layers are too optically thick for the laser to penetrate (an example distribution for winter 2020 over the Arctic is shown in Fig. 7a). The Mie channel measures winds under cloudy ~~or polluted~~ condition and thus has more measurements in the PBL than in the stratosphere (e.g., Fig. 7c). Furthermore, some ~~components of the~~ ascending and descending HLOS wind measurements cancel in the average owing to simply to the change of the angle of the LOS. ~~Therefore, to~~ To avoid this artefact and to add some insight into the wind features being measured, we also compare the projected HLOS wind vector into its zonal (positive to the east) and meridional (positive to the north) components ~~as~~. The distribution of the zonal-component of the HLOS winds is shown in Fig. 7e and g for Aeolus and ECCC-B HLOS winds. By doing this decomposition, the distributions for ascending and descending measurements are ~~more aligned~~brought into better agreement (Fig. 7f~~) and we~~). We also notice that the HLOS winds can ~~also~~ provide some information about the vertical variation of the HLOS winds that are projected onto the zonal direction (~~Fig. 7e and g). The distributions are positively skewed~~Figs. 7e and g). For example, for Aeolus the projection of HLOS into the zonal direction for the stratosphere, UTLS, and troposphere are +11.00 ms^{-1}, +4.00 ms^{-1} and +1.00 ms^{-1} respectively for this measurement period and these values (and the standard deviations of their distributions, see the figure legend for values) agree very well with ECCC-B (and ERA5 – not shown). The distributions have mean values that are positive because the winds are mainly westerly over the Arctic in the winter.

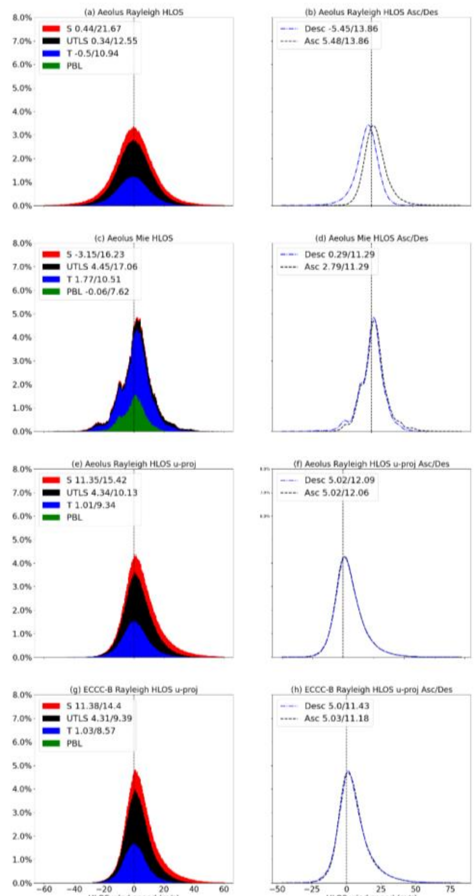
(a) Aeolus Rayleigh HLOS
S 0.44/21.67
UTLS 0.34/12.55
T -0.5/10.94
PBL
(b) Aeolus Rayleigh HLOS Asc/Des
Desc -5.45/13.86
Asc 5.48/13.86
(c) Aeolus Mie HLOS
S -3.15/16.23
UTLS 4.45/17.06
T 1.77/10.51
PBL -0.06/7.62
(d) Aeolus Mie HLOS Asc/Des
Desc 0.29/11.29
Asc 2.79/11.29
(e) Aeolus Rayleigh HLOS u-proj
S 11.35/15.42
UTLS 4.34/10.13
T 1.01/9.34
PBL
(f) Aeolus Rayleigh HLOS u-proj Asc/Des
Desc 5.02/12.09
Asc 5.02/12.06
(g) ECCC-B Rayleigh HLOS u-proj
S 11.38/14.4
UTLS 4.31/9.39
T 1.03/8.57
PBL
(h) ECCC-B Rayleigh HLOS u-proj Asc/Des
Desc 5.0/11.43
Asc 5.03/11.18
HLOS wind speed (m/s)
HLOS wind speed (m/s)

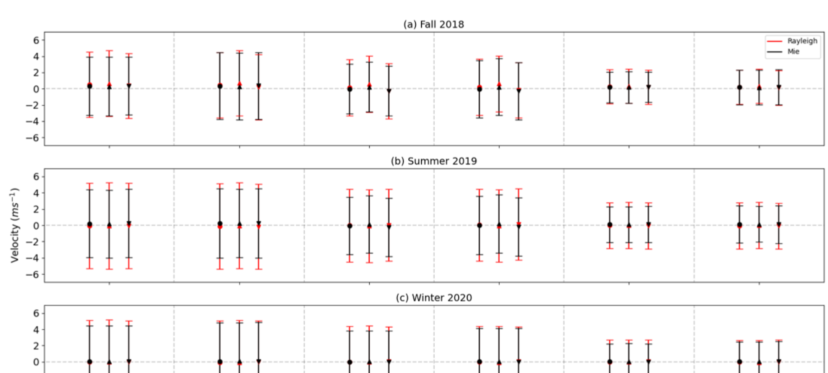
(a) Fall 2018
Rayleigh
Mie
(b) Summer 2019
Velocity (ms^{-1})
(c) Winter 2020

Figure ~~7.~~ **8.** Means and standard deviations of the distributions of the differences between Aeolus Rayleigh ~~((a) and (b))~~(Mie) winds and ~~Mie ((c) and (d)) HLOS measurement frequency distributions (%) during winter 2020~~ECCC-B and ERA5 shown as red (black) dots or triangles, and error bars, over the Arctic ~~(>70N)~~. ~~The HLOS winds are projected onto the east-west directions ((e) to (h)) from Aeolus measurements and ECCC-B HLOS winds. The panels on the right show the distribution of ascending and descending measurements separately. The means and standard deviations of distributions in each level are listed in the figure legends.~~

~~We compare the distributions of Aeolus, ECCC-B, and ERA5 winds during fall 2018, summer 2019, and winter 2020 over the Arctic, as summarized in Fig. 8, which shows the distributions of the HLOS winds, its zonal and meridional projections, and the zonal and meridional winds from the reanalysis. Since ECCC-B and ERA5 are mutually consistent, only the results from ECCC-B are displayed here. The standard deviations are indicated with horizontal bars. The measurements are decomposed into Rayleigh (blue) and Mie winds (black). They are further decomposed into ascending (indicated with upright triangles) and descending (inverted triangles) measurements. The last two columns in each panel represent the total zonal and meridional winds from ERA5. Both the observations and the model derived winds agree that aggregated HLOS winds have larger standard deviations than their zonal and meridional projected components. The large range on the HLOS distribution plots is controlled to an important extent by the systematic variation of the measurement angle: partially opposing HLOS winds can arise during ascending and descending orbits. Therefore, the means of all measurements (dots: including~~

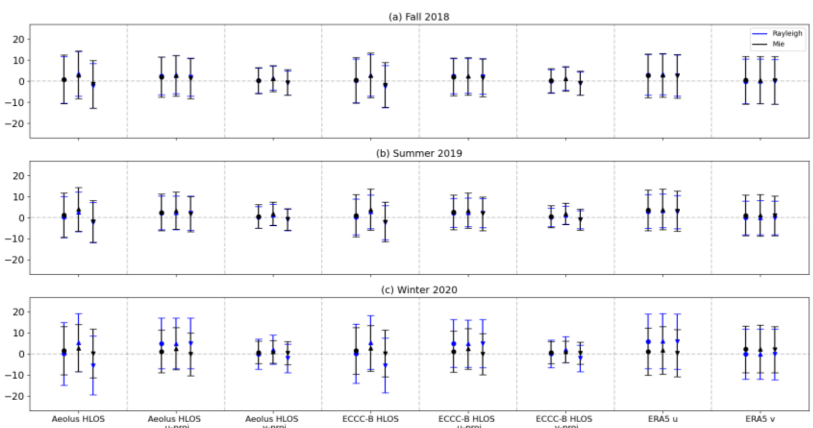

~~ascending and descending measurements) are generally somewhere between the means of ascending and descending measurements.~~

~~**Figure 8.** Means and standard deviations of Aeolus Rayleigh (blue) and Mie (black) HLOS winds, zonal and meridional components of Aeolus and ECCC-B HLOS winds, and zonal and meridional winds from the reanalysis ERA5, over the Arctic,~~ during (a) boreal fall 2018, (b) summer 2019, and (c) winter ~~2020 (c).~~2019-20. The dots represent Aeolus measurements in the atmosphere which can be decomposed into ascending (upright triangles) and descending (inverted triangles) measurements. The distributions of the differences of the projected winds are shown in the latter four columns.

Formatted: English (United Kingdom)

Formatted: Font: 9 pt, Bold, English (United States)

Formatted: Indent: First line: 0 cm, Line spacing: single

We compare the distributions of the differences between the Aeolus wind measurement data and the ECCC-B and ERA5 data during fall 2018, summer 2019, and winter 2020 over the Arctic, as summarized in Fig. 8, which shows the bias and standard deviations of the differences between Aeolus HLOS winds and the ECCC-B HLOS winds, and ERA5 HLOS winds, and their zonal and meridional projections. The measurements are decomposed into Rayleigh (red) and Mie winds (black). They are further decomposed into ascending (indicated with upright triangles) and descending (inverted triangles) measurements. ~~The averaged zonal and meridional winds from ERA5 at observation locations during ascending, descending, and both, are more aligned as expected. The standard deviations of the distributions of the zonal component of HLOS winds (columns 2 and 5) are similar to the ones from total zonal winds from ERA5 (column 7); however, the standard deviations of the meridional component of HLOS winds (columns 3 and 6) are about 50% smaller than the standard deviations of total meridional winds (column 8). For example, in winter 2020, the standard deviations of Aeolus Rayleigh and ERA5 HLOS v-projected winds are only 7.15 ms^{-1} and 6.64 ms^{-1}, but the standard deviation of the ERA5 meridional winds is as large as 11.95 ms^{-1}. Aeolus as designed provides mostly zonal information even over the Arctic.~~

The results, with the bias (the mean values of these differences for the different sampling used) being smaller than 0.7 ms^{-1}, are consistent with our bias correction method. The distributions of the differences in the ascending and descending measurements do not show a significant difference. The discrepancies in the meridional projections of the HLOS winds are smaller because Aeolus picks up mostly the zonal component of the winds due to the direction of the LOS.

Figure 8 shows an overall agreement between Aeolus, ECCC-B, and ERA5, ~~and~~but more analysis is required to bring out the differences between the datasets. One way to do so is to separately investigate the consistency between Aeolus and ECCC-B or ERA5 HLOS winds in the PBL, troposphere, UTLS, and stratosphere. Figure 9 shows normalized Taylor diagrams

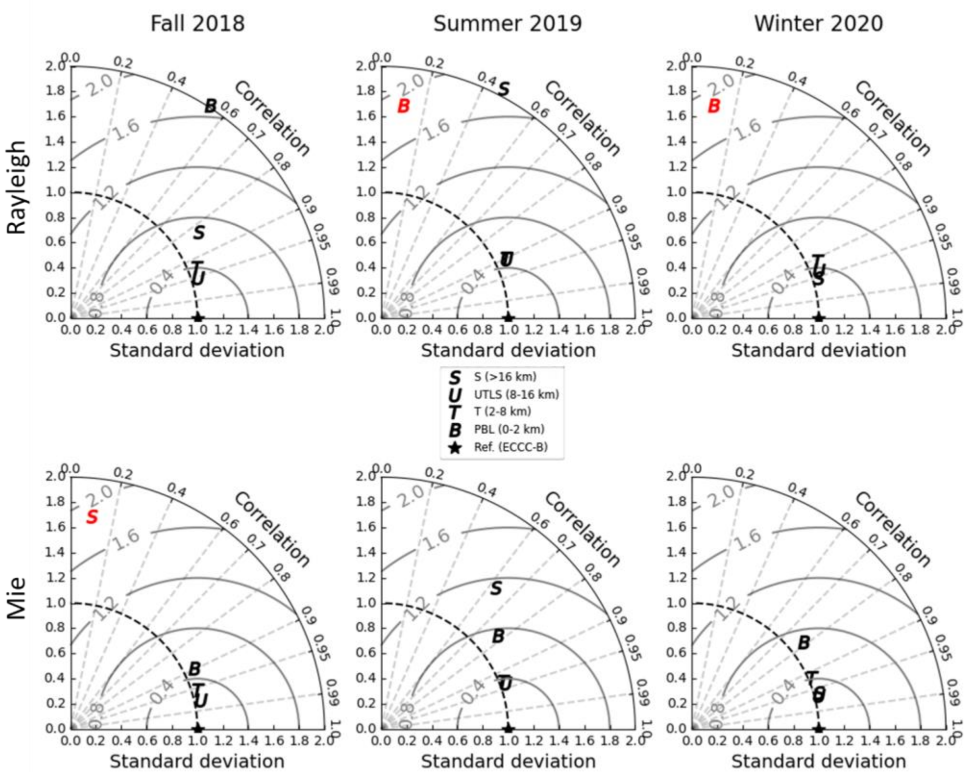

~~**Figure 9.** Normalized Taylor diagrams with ECCC-B as references for Aeolus measurements over the Arctic. The correlation coefficients and standard deviations are calculated for each layer. The angle indicates the correlation between Aeolus measurements and the reference. The distance to the origin represents the normalized standard deviation and to the star (reference) represents the normalized root-mean square error. Rows are distinguished by channels; columns are distinguished by seasons. The red markers on top left of panels represent layers with normalized standard deviations that are outside the range shown (> 2.2).~~

(Taylor, 2001), with ECCC-B as reference, for Aeolus Rayleigh and Mie measurements over the Arctic during the three seasons of analysis. ~~The Taylor diagrams with ERA5 as reference (not shown here) have nearly overlapping results because ERA5 and ECCC-B are mutually consistent.~~ The angle indicates the correlation between Aeolus measurements and ECCC-B. The distance to the origin represents the standard deviation and to the star (reference point (1,0)) represents the RMSD; both statistics are normalized by the standard deviation of reference data. The 1.0 normalized standard deviation is highlighted; data that falls outside the dashed quarter circle is noisier than the reference data. Figure 9 shows that Aeolus data

Formatted: Font: 9 pt, Bold, English (United States)

Formatted: Normal

Formatted: Font: 9 pt, English (United States)

Formatted: Font: 9 pt

Formatted: Font: Bold

Formatted: Indent: First line: 1.27 cm consistently has ~~more structure~~ greater standard deviations than ECCC-B during all three periods and for both Rayleigh and Mie winds~~. Its~~: its normalized standard deviations are ~~greater than those from ECCC-B by a factor of~~typically within 1.05 to 1.40. This might imply that Aeolus provides noisier data, that the ECCC-B is missing some extreme values in its wind-component distribution, or both. However, overall, the RMSD are generally within one normalized standard deviation and correlations are normally greater than 0.8. During the boreal summer period, the data in the stratosphere seem to agree less with the ECCC-B data, reflecting reduced sampling, solar background noise that is most effective during summer ~~as mentioned earlier~~, changes in the atmospheric environment in summer, thermal changes in the telescope, and other possible errors (Reitebuch et al., 2020).

Generally, the Rayleigh-clear channel provides consistent data with the ECCC-B through the troposphere (T in Fig. 9), the UTLS (U) and the stratosphere (S), while the Mie-cloudy channel provides consistency from the PBL (B) to the lower stratosphere. This reflects the vertical sampling and instrument characteristics and reveals effective complementarity of the instrument and retrieval design. For this reason, in the next paragraph, where we investigate the spatial distribution of the consistency in the lower and upper atmospheric regions, we exclude the Rayleigh winds in the PBL and the Mie winds in the stratosphere.

Formatted: English (United States)

Formatted: Indent: First line: 0 cm, Line spacing: single

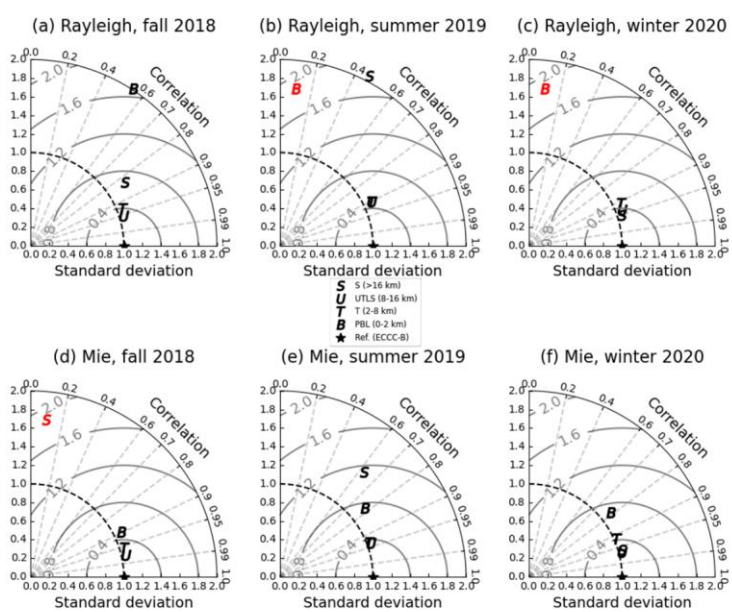

Figure 9. Normalized Taylor diagrams with ECCC-B as references for Aeolus measurements over the Arctic. The correlation coefficients and standard deviations are calculated for each layer. The angle indicates the correlation between Aeolus measurements and the reference. The distance to the origin represents the normalized standard deviation and to the star (reference) represents the normalized root-mean square error. Rows are distinguished by channels; columns are distinguished by seasons. The red markers on top left of panels represent layers with normalized standard deviations that are outside the range shown (> 2.2).

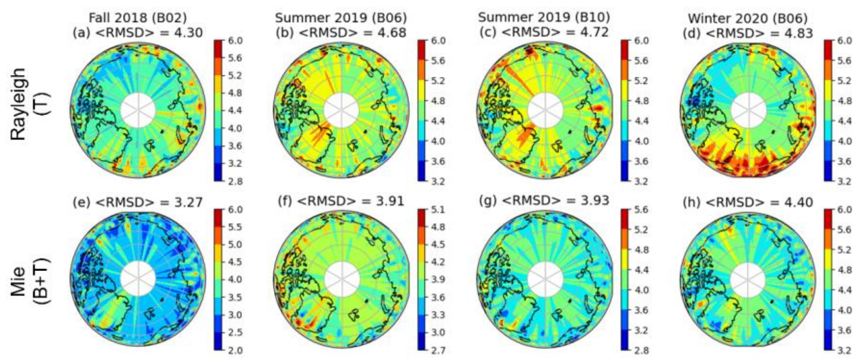

~~**Figure 10.** RMSD of Aeolus and ECCC-B vertical HLOS wind profiles for selected lower-atmospheric regions (Rayleigh T and Mie B+T) during fall 2018, summer 2019, and winter 2020.~~

Figure 10 shows the RMSD between Aeolus and ECCC-B for Rayleigh tropospheric (T) and Mie PBL + tropospheric (B+T) profiles, and Fig. 11 shows the same but for Rayleigh UTLS + stratosphere (U+S) and Mie UTLS (U) measurements. Since the estimated errors and RMSD were consistently decreasing in September 2019 over the Arctic except for the region with different range bin setting (Fig. 6), to avoid misinterpretation of the results on the maps, we exclude the data during this period over the entire Arctic. ~~The maps~~Since the measurement density differs depending on the latitude, the RMSD of the profiles are ~~plotted using~~ calculated over nearly equal surface area, ~~similar to the Lambert~~using the Equal-Area Scalable Earth (EASE) Grids (Brodzik et al., 2012). Each grid~~, with longitude grid of 3 degrees and latitude grid~~ cell is around 10^4 km^2 which is approximately the square of ~~inverse cosine~~the along-path resolution of ~~latitude degrees. For instance, a grid point at 60° N is 3° × 2° and a grid at 80° N is 3° × 5.7°. The averaged RMSD shown in angle brackets are simply the mean of the RMSD from all the grid cells.~~Aeolus Rayleigh winds. The first two and the last columns represent the distributions using the near real-time ~~2B06 dataset~~2B02/06/07 datasets; the third column shows the distributions using the reprocessed 2B10 data during the early FM-B period.

Formatted: Font: 9 pt, Bold, English (United States)

Formatted: Font: 9 pt

Formatted: Normal

Formatted: Font: 9 pt, English (United States)

Formatted: Font: Bold

Formatted: Font: 9 pt

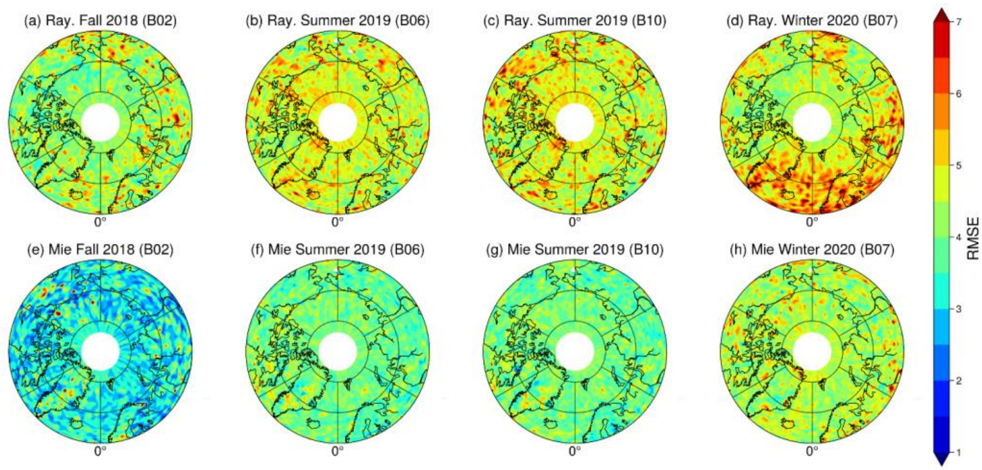

Figure 10. RMSD of Aeolus and ECCC-B vertical HLOS wind profiles for selected lower-atmospheric regions (Rayleigh T and Mie B+T) during fall 2018, summer 2019, and winter 2020.

Formatted: Font: 9 pt

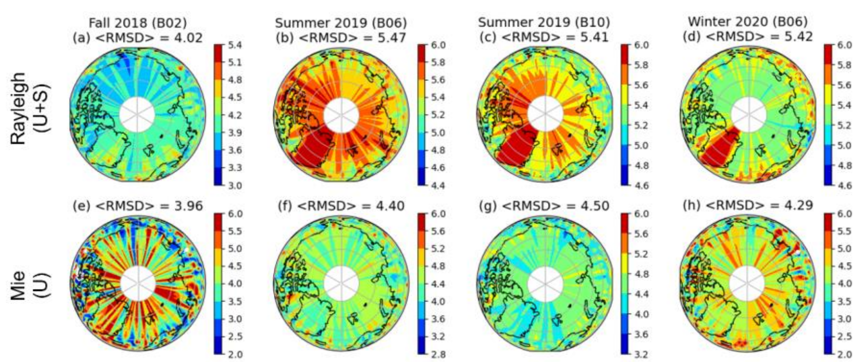

~~**Figure 11.** Similar to Figure 9, but for selected upper-atmospheric regions (Rayleigh U+S and Mie U).~~

Formatted: Indent: First line: 1.27 cm

The distributions of the RMSD in the lower atmosphere are relatively homogeneous across oceanic, ice-covered, and continental regions. This suggests that the overall good agreement seen for the in-situ Iqaluit and Whitehorse data as well as the ~~Northern~~northern Canadian region in the radiosonde network extends from land to the ocean regions without obvious systematic differences in consistency. The agreement between Aeolus and ECCC-B for the Mie winds is ~~greater~~better than for the Rayleigh winds for all three periods of analysis. The RMSD for the Mie winds largely lie between ~~3.~~2 ms^{-1} and 4~~.4 ms^{-1} in the lower atmosphere and between 3.9 ms^{-1} and 4.5 ms^{-1} in the upper atmosphere~~ ms^{-1}, and for Rayleigh winds, ~~between 4.3 ms^{-1} and 4.9 ms^{-1} in the lower atmosphere and between 4.0 ms^{-1} and 5.5 ms^{-1} aloft~~the RMSD are generally greater than 4 ms^{-1}. This was anticipated because the Rayleigh winds are noisier for reasons alluded to above. The RMSD ~~does not vary~~are systematically ~~between~~greater in the lower-atmosphere ~~and~~than in the upper-atmosphere ~~comparisons~~as shown in ~~Fig~~Figs. 10 and 11, ~~but~~and the differences could be anticipated from the estimated error product (as shown in ~~Fig. S2~~Figs. S1 and ~~S3). For example, estimated errors were comparable in the upper and lower atmosphere layers for the Fall 2018 data, were greater for both layers for Summer 2019, and were greater in the upper atmosphere than in the lower atmosphere for Summer 2019. These same characteristics generally apply to the RMSD statistics.~~S2).

~~During winter 2020, the observation errors were greater (around 3.6 ms^{-1}) from the Southern Greenland to North-western Russia in the lower atmosphere, which corresponds to the region with RMSD around 6.0 ms^{-1} between Aeolus Rayleigh winds and ECCC-B. By the same token, the estimated errors were greater during the summer 2019 over the Greenland and oceanic region (around 6.9 ms^{-1}), and during the winter 2020 over the Greenland (around 3.9 ms^{-1}) in the upper atmosphere. Whatever~~In the upper atmosphere, the RMSD are significantly larger for the Rayleigh winds during FM-B period, especially over Greenland where the RMSD are greater than 6.0 ms^{-1}. This might be caused by the reflection from the Greenland ice sheet which leads to enhanced errors. The estimated errors also show a similar pattern: the estimated error over Greenland in summer 2019 is around 6.0 ms^{-1} (Fig. S2b), the reprocessed product reduced the estimated error to around 5.0 ms^{-1} (Fig. S2c), and it is around 4.0 ms^{-1} during winter 2020 (Fig. S2d) due to the lack of solar background noise in the boreal winter. This pattern is however not seen during the FM-A period. But whatever the source of these changes (e.g., summertime solar background noise amplification or calibration errors coinciding with the start of laser-B stream), it is noteworthy that the estimated error product contains potentially useful information for validation purposes. Because such information is useful for error characterization in NWP, as we will discuss below, a more detailed investigation into the estimated error product, including its seasonal, geographic, and flow dependence, is warranted.

Formatted: Left, Indent: First line: 0 cm

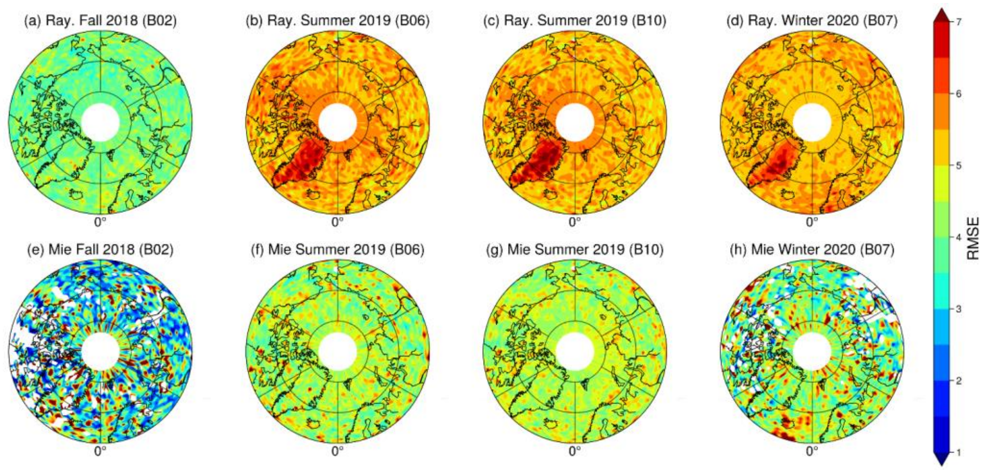

Figure 11. Similar to Figure 9, but for selected upper-atmospheric regions (Rayleigh U+S and Mie U).

Formatted: Indent: First line: 1.27 cm

Note that the first reprocessed data, 2B10, only overlaps with one of the three periods of study: August to September 2019. The estimated observational errors have decreased compared to the 2B06 data (Figs. S1 and S2) since the bias due to the M1 mirror temperature ~~dependent has been corrected~~dependence is updated on a daily basis and the dark current signals have been removed using ~~a better~~improved quality control. ~~The third columns in Fig. 10 to 11 show~~However, we do not see the ~~RMSD~~same improvement in the O-B statistics between ~~the Aeolus reprocessed data and the ECCC-B vertical HLOS wind profiles~~2B06 and ~~during the summer 2019. No significant improvement is seen here because we have implemented a weekly updated dynamic bias correction to the near real time data. Nevertheless, the reprocessed data will help inter-comparison within weather centers for their NWP experiments since it does not need further bias correction on the L2B~~2B10 products over the Arctic region.

4 Summary and conclusion

In August 2018, ESA successfully launched the first spaceborne DWL Aeolus to measure global wind profile measurements along its LOS, using the instrument's Rayleigh and Mie channel receivers. Only Rayleigh-clear winds and Mie-cloudy winds are considered in the validation. In this work, the Aeolus data product are bias corrected and quality controlled using the quality flag from the L2B product, estimated error screening following ECMWF's guidance, and the screening when O-B is greater than 30 ms^{-1} to remove any additional outliers. Our results show consistent Aeolus data products around the sites with the 9-h short-range forecast from ECCC ("background", ECCC-B), reanalysis ERA5 from ECMWF, and in-situ measurements using radiosondes and Ka-band radar, for the period 15 September ~~15th~~ to 16 October ~~16th,~~ 2018. For example, the adjusted r-squared between Aeolus Rayleigh winds and ECCC-B is 0.92, and 0.91 between Aeolus and ERA5 at the Iqaluit site. For the Aeolus Mie winds, the statistical results are 0.87 with ECCC-B and 0.81 with ERA5. The comparison with the Ka-band radar at Iqaluit has been limited to the early phase of Aeolus lifetime due to some technical issues from the ground-based radar. The agreement between Aeolus wind product and the Ka-band radar is systematically worse than with the forecasts and reanalysis products. ~~Possible issues include: the radar provides more localized measurements than Aeolus, the radar's sampling is very limited, and the winds at lower altitudes, where the radar samples winds, are greatly influenced by the topography. As a result, the adjusted r-squared between Aeolus winds and the Ka-band radar are 0.53 for the Rayleigh winds and 0.66 for the Mie winds. Nevertheless, we were able to~~We acknowledge the little overlap data with Aeolus due to the radar's limited sampling, but the comparison between Aeolus and radar, which are totally independent, is still at 99% confidence level using F-test. This provides encouragement for programs like CAWS to enhance independent radar measurements over Canadian Arctic sites. We also validate Aeolus wind products with ECCC-B, ERA5, and radiosonde measurements around other radiosonde sites for the periods 15 September ~~15th~~ to 16 October ~~16th,~~ 2018, 2 August ~~2nd~~ to 30 September ~~30th,~~ 2019, and 1 December ~~1st~~ to 31 January ~~31st,~~ 2020. This comparison raises the issue of solar background noise at high latitudes during summertime, which degrades the adjusted r-squared of the Rayleigh winds by about 10% during the early FM-B period (Fig. 5). This issue extends to the analysis of the pan-Arctic, where the effect of solar background radiation is even larger over polar regions where there are 24 hours periods of sunlight in summer (~~Fig~~Figs. 11b-c).

~~In our analysis of the pan-Arctic region, Taylor diagrams~~In our analysis of the pan-Arctic region, we found an overall agreement by comparing the distributions of the HLOS winds, ascending and descending HLOS winds, and projections of HLOS winds onto east-west and north-south directions in different atmospheric layers (Fig. 7), and we also compared the distributions of the differences between Aeolus and ECCC-B and ERA5 (Fig. 8). Due to the angle of the HLOS, when comparing the distributions, separating the ascending with descending measurements helps avoid cancelling out part of the HLOS winds and projecting the HLOS winds on to zonal and meridional directions provides some insight on the vertical variation of the HLOS winds. To further investigate the consistency, we showed normalized Taylor diagrams in Fig. 9, which reveal that the standard deviations of Aeolus winds are 5 to 40% greater than ECCC-B in every layer. Future work could investigate whether this discrepancy arises because Aeolus provides noisier measurements due to limitations of the processed observations or because Aeolus is measuring structural detail not captured in the forecast and reanalysis. ~~Yet, they show~~In any case, this analysis reveals consistent HLOS winds with correlations higher than 0.8 except during summer in the stratosphere and normalized standard errors within one standard deviation of ECCC-B. Finally, the spatial ~~correlations~~RMSD of Aeolus and ECCC-B vertical wind profiles confirm their mutual consistency. We ~~have~~ found ~~some initial evidence~~ that the spatial variability of the time-averaged L2B estimated error product is ~~also a~~in good ~~predictor of~~ agreement with the spatial variability of the RMSD between Aeolus and ~~the reanalysis, which could be useful~~ ECCC-B HLOS winds over the Arctic region. This validates the use of L2B estimated error product as a predictor for ~~constraining future~~the HLOS wind observation errors in data assimilation systems, as proposed by Rennie et al. (2021), to obtain optimal positive impacts on forecasts from assimilating Aeolus winds.

In conclusion, the mutual consistency between Aeolus and the short-range forecast and reanalysis over the Arctic suggests that Aeolus provides reliable wind measurements that can further advance our knowledge on circulation and further improve current NWP models, and also suggests that the ERA5 reanalysis and ECCC-B provide good estimates of the circulation over the Arctic, reflecting the volume of satellite data assimilated daily (over 1 million observations, mainly radiances) and mass balance constraints that hold at high latitudes. It remains open, however, how the consistency between Aeolus and available analyzed data depends on horizontal and vertical scale. It is reassuring that this consistency is seen in a vertical range extending from the planetary boundary layer in the Mie channel in all three observation periods to the stratosphere in the Rayleigh channel (in the non-summer periods). The promise of added value to forecasts from Aeolus winds is already being borne out at several centers that have assimilated Aeolus data into their operational NWP model and are seeing positive impact (e.g., Rennie ~~and Isaksen, 2020~~et al., 2021). A focus on predictability of weather systems in the Arctic, and on predictability from wind information centred in the Arctic, is the subject of current work.

Data availability

The Ka-band radar at Iqaluit and ECCC-B data used in this paper can be provided by the corresponding author (gina.chou@mail.utoronto.ca) upon request. The ERA5 data can be downloaded from the Copernicus Climate Change Service (C3S) Climate Date Store (https://cds.climate.copernicus.eu/cdsapp#!/dataset/reanalysis-era5-pressure-levels?tab=overview). The radiosondes data can be downloaded from http://weather.uwyo.edu/upperair/sounding.html. Aeolus L2B data can be obtained from the VirES visualization tool (https://aeolus.services/).

Author contribution

Chih Chun Chou prepared the main part of the paper and performed the statistical analyses of Aeolus data, in-situ measurements, ECCC-B, and ERA5 data. Paul Kushner and Stéphane Laroche guided Chih Chun Chou for the analyses and the written part. Stéphane Laroche provided the ECCC-B data and Zen Mariani provided the in-situ measurements at Iqaluit and Whitehorse supersites. Zen Mariani, Peter Rodriguez, and Stella Melo provided guidance in reading and retrieving the radar data. All co-authors helped review the manuscript.

Competing interests

The authors declare that they have no conflict of interest.

Acknowledgements

We acknowledge ESA for the Aeolus data, ECMWF for the ERA5 data, and ECCC for the short-range forecast and in-situ measurements. We ~~are also very grateful to~~acknowledge the support of the Canadian Space ~~Agency for the funding~~Agency's Earth System Science Data Analysis program.

References

Baars, H., Herzog, A., Heese, B., Ohneiser, K., Hanbuch, K., Hofer, J., Yin, Z., Engelmann, R., and Wandinger, U.: Validation of Aeolus wind products above the Atlantic Ocean, Atmos. Meas. Tech., 13, 6007–6024, https://doi.org/10.5194/amt-13-6007-2020, 2020.

Baker, W. E. et al.: Lidar measured winds from space: A key component for weather and climate. – Bull. Amer. Meteor. Soc. 76, 869–888, 1995.

Bormann N, Thépaut J-N: Impact of MODIS polar winds in ECMWF's 4D-VAR data assimilation system. Mon. Weather Rev. 132: 929–940, 2004.

Belova, E., Kirkwood, S., Voelger, P., Chatterjee, S., Satheesan, K., Hagelin, S., Lindskog, M., and Körnich, H.: Validation of Aeolus winds using ground-based radars in Antarctica and in northern Sweden, Atmos. Meas. Tech~~.~~ ~~Discuss. [preprint],~~., 14, 5415–5428, https://doi.org/10.5194/amt-14-5415-2021~~-54, in review~~, 2021.

Brodzik MJ, Billingsley B, Haran T, Raup B, Savoie MH.: *EASE-Grid 2.0*: Incremental but Significant Improvements for Earth-Gridded Data Sets. *ISPRS International Journal of Geo-Information*. 2012; 1(1):32-45. https://doi.org/10.3390/ijgi1010032.

Buehner, M. et al.: Implementation of Deterministic Weather Forecasting Systems Based on Ensemble–Variational Data Assimilation at Environment Canada. Part I: The Global System. Mon. Wea. Rev., 143, 2532–2559, https://doi.org/10.1175/MWR-D-14-00354.1, 2015.

Chiara, G. D., M. Bonavita and S. J. English: Improving the Assimilation of Scatterometer Wind Observations in Global NWP, in IEEE Journal of Selected Topics in Applied Earth Observations and Remote Sensing, vol. 10, no. 5, pp. 2415-2423, doi: 10.1109/JSTARS.2017.2691011, 2017.

Cohen, J., Zhang, X., Francis, J. et al.: Divergent consensuses on Arctic amplification influence on midlatitude severe winter weather. Nat. Clim. Chang. 10, 20–29, https://doi.org/10.1038/s41558-019-0662-y, 2020.

Dabas, A: Observing the atmospheric wind from space. CR Geosci., 342, 370–379, 2010.

de Kloe, J., Stoffelen, A., Tan, D., Andersson, E., Rennie, M., Dabas, A., Poli, P., and Huber, D.: ADM-Aeolus Level-2B/2C Processor Input/Output Data Definitions Interface Control Document, https://earth.esa.int/pi/esa?type=file&table=aotarget&cmd=image&alias=ADM_Aeolus_L2B_Input_Output_DD_ICD, last access: 3 November 2020, 2016.

Dirksen, R. J., Sommer, M., Immler, F. J., Hurst, D. F., Kivi, R., and Vömel, H.: Reference quality upper-air measurements: GRUAN data processing for the Vaisala RS92 radiosonde, Atmos. Meas. Tech., 7, 4463–4490, https://doi.org/10.5194/amt-7-4463-2014, 2014.

Drinkwater, M., M. Borgeaud, A. Elfving, P. Goudy, W. Lengert: ADM-Aeolus Mission Requirements Document. Mission Science Division, AE-RP-ESA-SY-001 EOP-SM/2047, 2016.

Fehr, T., Amiridis, V., Bley, S., Cocquerez, P., Lemmerz, C., Močnik, G., Skofronick-Jackson, G., and Straume, A. G.: Aeolus Calibration, Validation and Science Campaigns , EGU General Assembly 2020, Online, 4–8 May 2020, EGU2020-19778, https://doi.org/10.5194/egusphere-egu2020-19778, 2020.

Graham, R. J., Anderson, S. R., & Bader, M. J.: The relative utility of current observation systems to global-scale NWP forecasts. Quarterly Journal of the Royal Meteorological Society, 126(568), 2435–2460. https://doi.org/10.1002/qj.49712656805, 2020.

Guo, J., Liu, B., Gong, W., Shi, L., Zhang, Y., Ma, Y., Zhang, J., Chen, T., Bai, K., Stoffelen, A., de Leeuw, G., and Xu, X.: Technical Note: First comparison of wind observations from ESA's satellite mission Aeolus and ground-based Radar wind profiler network of China, Atmos. Chem. Phys. Discuss., https://doi.org/10.5194/acp-2020-869, in review, 2020.

Horányi, A., C. Cardinali, M. Rennie, and L. Isaksen: The assimilation of horizontal line-of-sight wind information into the ECMWF data assimilation and forecasting system. Part I: The assessment of wind impact. Quart. J. Roy. Meteor. Soc., 141, 1223–1232, https://doi.org/10.1002/qj.2430, 2015.

Hersbach, H., Bell, B., Berrisford, P., et al.: The ERA5 global reanalysis. Q J R Meteorol Soc. 2020; 146: 1999– 2049. https://doi.org/10.1002/qj.3803, 2020.

Hersbach, H., P. de Rosnay, B. Bell, D. Schepers, A. Simmons, C. Soci, S. Abdalla, M. Alonso Balmaseda, G. Balsamo, P. Bechtold, P. Berrisford, J. Bidlot, E. de Boisséson, M. Bonavita, P. Browne, R. Buizza, P. Dahlgren, D. Dee, R. Dragani, M. Diamantakis, J. Flemming, R. Forbes, A. Geer, T. Haiden, E. Hólm, L. Haimberger, R. Hogan, A. Horányi, M. Janisková, P. Laloyaux, P. Lopez, J. Muñoz-Sabater, C. Peubey, R. Radu, D. Richardson, J.-N. Thépaut, F. Vitart, X. Yang, E. Zsótér & H. Zuo: Operational global reanalysis: progress, future directions and synergies with NWP, ECMWF ERA Report Series 27, 2018.

Joe, P., ~~Melon~~Melo, S., Burrows, W., Casati, B., Crawford, R.W., Deghan, A., Gascon, G., Mariani, Z., Milbrandt, J., Strawbridge, K.: The Canadian Arctic Weather Science Project: Introduction to the Iqaluit Site. Bull. Am. Met. Soc., 101, E109-E128, https://doi.org/10.1175/BAMS-D-18-0291.1, 2020.

Källen, E.: Scientific motivation for ADM-Aeolus mission, EPJ Web of Conferences, 176, 02 008, https://doi.org/10.1051/epjconf/201817602008, 2018.

Kanitz, T., Lochard, J., Marshall, J., McGoldrick, P., Lecrenier, O., Bravetti, P., Reitebuch, O., Rennie, M., Wernham, D., and Elfving, A.: Aeolus first light: first glimpse, in: International Conference on Space Optics – ICSO 2018, 9– 12 October 2018, Chania, Greece, vol. 11180, 659–664, https://doi.org/10.1117/12.2535982, 2019.

Krisch, I., C. Lemmerz, O. Lux, U. Marksteiner, O. Reitebuch, F. Weiler, B. Witschas, F. Bracci, M. Meringer, K. Schmidt, D. Huber, I. Nikolaus, M. Vaughan, A. Dabas, T. Flament, D. Trapon, S. Abdalla, L. Isaksen, M. Rennie, D. Donovan, J. de Kloe, G.-J. Marseille, A. Stoffelen, T. Kanitz, A.-G. Straume, D. Wernham, J. von Bismarck, S. Bley, P. Fischer, T. Parinello: Data quality of Aeolus wind measurements. In: Geophysical Research Abstracts. EGU General Assembly 2020, 04.-08. Mai 2020, Wien, Österreich. DOI: 10.5194/egusphere-egu2020-9471, 2020.

Laroche, S. and J. St-James: Impact of the Aeolus L2B HLOS winds in the ECCC global forecast system. Submitted to *Quarterly Journal of the Royal Meteorological Society*, 2021.

Laroche, S., J. Blezius, J. St-James: Validation of HLOS Winds With ECCC Global Deterministic Short-range Forecasts. Aeolus CAL/VAL and Science Workshop, Frascati, 2019.

Laroche, S., and R. Sarrazin: Impact of Radiosonde Balloon Drift on Numerical Weather Prediction and Verification. *Weather and Forecasting* 28, 3, 772-782, 2013.

Lawrence, H., N. Bormann, I. Sandu, J. Day, J. Farnan, P. Bauer: Use and impact of Arctic observations in the ECMWF Numerical Weather Prediction system. Q J R Meteorol Soc.; 145: 3432– 3454. https://doi.org/10.1002/qj.3628, 2019.

Le Marshall, J., J. Jung, T. Zapotocny, C. Redder, M. Dunn, J. Daniels, and L. P. Riishojgaard: Impact of MODIS atmospheric motion vectors on a global NWP system. Aust. Meteor. Mag., 57, 45–51, 2008.

Lhermitte, R. M., and D. Atlas: Precipitation motion by pulse Doppler radar. Proc. Ninth Weather Radar Conf., Kansas City, MO, Amer. Meteor. Soc., 218–223, 1962.

Lux, O., D. Wernham, P. Bravetti, P. McGoldrick, O. Lecrenier, W. Riede, A. D'Ottavi, V.D. Sanctis, M. Schillinger, J. Lochard, J. Marshall, C. Lemmerz, F. Weiler, L. Mondin, A. Ciapponi, T. Kanitz, A. Elfving, T. Parrinello, and O. Reitebuch: High-power and frequency-stable ultraviolet laser performance in space for the wind lidar on Aeolus, Opt. Lett. 45, 1443-1446, 2020.

Mariani, Z., Crawford, R., Casati, B., Lemay, F.: A Multi-Year Evaluation of Doppler Lidar Wind-Profile Observations in the Arctic. *Remote Sens. 12*, 323. https://doi.org/10.3390/rs12020323, 2020.

Mariani, Z., Dehghan, A., Gascon, G., Joe, P., Hudak, D., Strawbridge, K., & Corriveau, J.: Multi-instrument observations of prolonged stratified wind layers at Iqaluit, Nunavut. Geophysical Research Letters, 45, 1654–1660. https://doi.org/10.1002/2017GL076907, 2018.

Martin, A., Weissmann, M., Reitebuch, O., Rennie, M., Geiß, A., and Cress, A.: Validation of Aeolus winds using radiosonde observations and ~~NWP~~numerical weather prediction model equivalents, Atmos. Meas. Tech~~. Discuss.,~~., 14, 2167–2183, https://doi.org/10.5194/amt-~~2020-404, in review, 2020~~14-2167-2021, 2021.

McTaggart-Cowan, R., Vaillancourt, P. A., Zadra, A., Chamberland, S., Charron, M., Corvec, S., et al.: Modernization of atmospheric physics parameterization in Canadian NWP. Journal of Advances in Modeling Earth Systems, 11, https://doi.org/10.1029/2019MS001781, 2019.

Mizyak, V.G., Shlyaeva, A.V., and Tolstykh, M.A.: Using satellite-derived Atmospheric Motion Vector (AMV) observations in the ensemble data assimilation system. Russ. Meteorol. Hydrol. 41, 439-446, https://doi.org/10.3103/S1068373916060091, 2016.

Naakka, T., T. Nygård, M. Tjernström, T. Vihma, R. Pirazzini, and I. M. Brooks: The impact of radiosounding observations on numerical weather prediction analyses in the arctic, Geophys. Res. Lett., vol. 46, no. 14, p. 46, 2019.

Reitebuch, O., I, Krisch, C. Lemmerz, O. Lux, U. Marksteiner, N. Masoumzadeh, F. Weiler, B. Witschas, F. Bracci, M. Meringer, K. Schmidt, D. Huber, I. Nikolaus, F. Fabre, M. Vaughan, K. Reissig, A. Dabas, T. Flament, A. Lacour, T. Parrinello: Assessment of the Aeolus performance and bias correction - results from the Aeolus DISC, Online, Aeolus Cal/Val and Science Workshop, http://elib.dlr.de/138648/, 2020.

Reitebuch, O., Lemmerz, C., Lux, O., Marksteiner, U., Rahm, S., Weiler, F., Witschas, B., Meringer, M., Schmidt, K., Huber, D., Nikolaus, I., Geiss, A., Vaughan, M., Dabas, A., Flament, T., Stieglitz, H., Isaksen, L., Rennie, M., de Kloe, J., Marseille, G.- J., Stoffelen, A., Wernham, D., Kanitz, T., Straume, A.-G., Fehr, T., von Bismark, J., Floberghagen, R., and Parrinello, T.: Initial assessment of the performance of the first Wind Lidar in space on Aeolus, in: International Laser Radar Conference, Hefei, China, 24–28 June 2019.

~~Rennie, M. and Isaksen, L.: Guidance for Aeolus NWP Impact Experiments during the period September 2018 to November 2019. Updated information to Aeolus CAL/VAL PIs performing NWP Impact Assessment Experiments, 2019.~~

Rennie, M.P., Isaksen, L., Weiler, F., de Kloe, J., Kanitz, T. & Reitebuch, O.: The impact of Aeolus wind retrievals on ECMWF global weather forecasts. Q J R Meteorol Soc, 147, 740, 3555– 3586. Available from: https://doi.org/10.1002/qj.4142, 2021.

Rennie, M. and Isaksen, L.: The NWP Impact of Aeolus Level-2B Winds at ECMWF, https://www.ecmwf.int/sites/default/files/elibrary/2020/19538-nwp-impact-aeolus-level-2b-winds-ecmwf.pdf, last access: 5 November 2020, 2020.

Rennie, M., Tan, D., Andersson, E., Poli, P., Dabas, A., De Kloe, J., Marseille, G.-J., and Stoffelen, A.: Aeolus Level-2B Algorithm Theoretical Basis Document (Mathematical Description of the Aeolus L2B Processor), https://earth.esa.int/pi/esa?type=file&table=aotarget& cmd=image&alias=Aeolus_L2B_Algorithm_TBD, last access: 3 November 2020, 2020a.

Sato, K., J. Inoue, A. Yamazaki, J.-H. Kim, M. Maturilli, K. Dethloff, S. R. Hudson, and M. A. Granskog: Improved forecasts of winter weather extremes over midlatitudes with extra Arctic observations, J. Geophys. Res. Oceans, 122, 775–787, doi:10.1002/ 2016JC012197, 2017.

Straume, A. G., and Coauthors: Aeolus Sensor, Data Processing and Product Description. Aeolus CAL/VAL community, 28 October 2018, 2018.

Taylor, K. E.: Summarizing multiple aspects of model performance in a single diagram, J. Geophys. Res., 106(D7), 7183– 7192, doi:10.1029/2000JD900719, 2001.

Velden, C. S., C. M. Hayden, S. J. Nieman, W. P. Menzel, S.Wanzong, and J. S. Goerss: Upper-tropospheric winds derived from geostationary satellite water vapor observations. Bull. Amer. Meteor. Soc., 78, 173–195, doi:10.1175/ 1520-0477(1997)078,0173:UTWDFG.2.0.CO;2, 1997.

Velden, C., W. E. Lewis, W. Bresky, D. Stettner, J. Daniels, and S. Wanzong: Assimilation of High-Resolution Satellite-Derived Atmospheric Motion Vectors: Impact on HWRF Forecasts of Tropical Cyclone Track and Intensity. Mon. Wea. Rev., 145, 1107–1125, https://doi.org/10.1175/MWR-D-16-0229.1, 2017.

Walsh, J.E., T.J. Ballinger, E. S. Euskirchen, E. Hanna, J. Mård, J.E. Overland, H. Tangen, T. Vihma: Extreme weather and climate events in northern areas: A review, Earth-Science Reviews, Volume 209, 103324, ISSN 0012-8252, https://doi.org/10.1016/j.earscirev.2020.103324, 2020.

Wang, Z., Z. Liu, L. Liu, S. Wu, B. Liu, Z. Li, and X. Chu: Iodine-filter-based mobile Doppler lidar to make continuous and full-azimuth-scanned wind measurements: data acquisition and analysis system, data retrieval methods, and error analysis, Appl. Opt. 49, 6960-6978, 2010.

Wright, C. J., Hall, R. J., Banyard, T. P., Hindley, N. P., Mitchell, D. M., and Seviour, W. J. M.: Dynamical and Surface Impacts of the January 2021 Sudden Stratospheric Warming in Novel Aeolus Wind Observations, MLS and ERA5, Weather ~~Clim. Dynam. Discuss. [preprint],~~and Climate Dynamics, https://doi.org/10.5194/wcd-2021-16~~, in review~~, 2021.

Young, I. R., Sanina, E., and Babanin, A. V.: Calibration and Cross Validation of a Global Wind and Wave Database of Altimeter, Radiometer, and Scatterometer Measurements. Journal of Atmospheric and Oceanic Technology 34, 1285–1306, 2017.

Yamazaki, A, Inoue, J, Dethloff, K, Maturilli, M, and König-Langlo, G: Impact of radiosonde observations on forecasting summertime Arctic cyclone formation. J. Geophys. Res. Atmos., 120, 3249– 3273. doi: 10.1002/2014JD022925, 2015.

Zhang, C., X. Sun, R. Zhang, S. Zhao, W. Lu, Y. Liu, and Z. Fan: Impact of solar background radiation on the accuracy of wind observations of spaceborne Doppler wind lidars based on their orbits and optical parameters, Opt. Express 27, A936-A952, 2019.

Zhang, C., X. Sun, W. Lu, Y. Shi, N. Dou, and S. Li.: On the relationship between wind observation accuracy and the ascending node of sun-synchronous orbit for the Aeolus-type spaceborne Doppler wind lidar, Atmos. Meas. Tech. Discuss., https://doi.org/10.5194/amt-2020-202, 2020.